Engineering supramolecular dynamics of self-assembly and turnover of oncogenic microRNAs to drive their synergistic destruction in tumor models

DOI:
10.1016/j.biomaterials.2024.122604

Document Version
Final published version

Biomaterials 309 (2024) 122604

Contents lists available at ScienceDirect

Biomaterials

journal homepage: www.elsevier.com/locate/biomaterials

Engineering supramolecular dynamics of self-assembly and turnover of oncogenic microRNAs to drive their synergistic destruction in tumor models

Daria Chiglintseva [b], David J. Clarke [a], Aleksandra Sen'kova [b], Thomas Heyman [a], Svetlana Miroshnichenko [b], Fangzhou Shan [a], Valentin Vlassov [b], Marina Zenkova [b], Olga Patutina [b,**,1], Elena Bichenkova [a,*]

[a] School of Health Sciences, Faculty of Biology, Medicine and Health, University of Manchester, Oxford Road, Manchester, M13 9PT, UK
[b] Institute of Chemical Biology and Fundamental Medicine SB RAS, 8 Lavrentiev Avenue, 630090, Novosibirsk, Russia

ARTICLE INFO

Keywords:
Artificial enzyme
Supramolecular dynamics
Catalytic turnover
Oncogenic miRNA
Antitumor therapy
RNase H

ABSTRACT

Rationally-engineered functional biomaterials offer the opportunity to interface with complex biology in a predictive, precise, yet dynamic way to reprogram their behaviour and correct shortcomings. Success here may lead to a desired therapeutic effect against life-threatening diseases, such as cancer. Here, we engineered "Crab"-like artificial ribonucleases through coupling of peptide and nucleic acid building blocks, capable of operating alongside and synergistically with intracellular enzymes (RNase H and AGO2) for potent destruction of oncogenic microRNAs. "Crab"-like configuration of two catalytic peptides ("pincers") flanking the recognition oligonucleotide was instrumental here in providing increased catalytic turnover, leading to ≈30-fold decrease in miRNA half-life as compared with that for "*single-pincer*" conjugates. Dynamic modeling of miRNA cleavage illustrated how such design enabled "Crabs" to drive catalytic turnover through simultaneous attacks at different locations of the *RNA-DNA* heteroduplex, presumably by producing smaller cleavage products and by providing toeholds for competitive displacement by intact miRNA strands. miRNA cleavage at the 5′-site, spreading further into double-stranded region, likely provided a synergy for RNase H1 through demolition of its loading region, thus facilitating enzyme turnover. Such synergy was critical for sustaining persistent disposal of continually-emerging oncogenic miRNAs. A single exposure to the best structural variant (Crab-p-21) prior to transplantation into mice suppressed their malignant properties and reduced primary tumor volume (by 85 %) in MCF-7 murine xenograft models.

1. Introduction

The complexity of biological systems and challenges associated with their regulation, manipulation or correction, to reprogram their behaviour and achieve desired therapeutic outcomes, require accuracy and precision, both at the level of biological recognition and during 3D self-assembly of the key functional players to maximize their action. This often requires engineering of "smart" biomaterials with highly-controlled chemical and physical properties that can be modelled, rationally designed and chemically synthesized in order to produce new biological functionalities, not found in nature. Such biomaterials incorporate several responsive functional domains, each with unique roles, traits and physicochemical characteristics, which are capable of communicating with each other and with the target components of living systems through a network of anticipated molecular interactions in a dynamic and responsive manner. Peptide and nucleic acid building blocks are widely used in biomaterials due to their highly-predictable network of atomic interactions, which offers dynamic control of their structure, shape and function. Their covalent coupling can produce a new, biologically-active material to leverage the unique advantages of each component and offer the opportunities to reprogram their interactions with complex biological systems and correct shortcomings.

* Corresponding author.
** Corresponding author.
E-mail addresses: patutina@niboch.nsc.ru (O. Patutina), elena.v.bichenkova@manchester.ac.uk (E. Bichenkova).
[1] Contributing equally

https://doi.org/10.1016/j.biomaterials.2024.122604
Received 10 December 2023; Received in revised form 11 April 2024; Accepted 5 May 2024
Available online 6 May 2024

Ultimately, this may lead to biological and clinical benefits. Success here may offer a basis for therapeutic innovation for precise and potent treatment of debilitating or life-threatening human pathologies, such as cancer.

Malignant transformation leading to development of various oncological diseases is a complex process, closely associated with impaired regulatory pathways of gene expression. MicroRNAs (miRNAs) are known to wield major influence over post-transcriptional gene regulation. By base pairing with the 3′-untranslated region in the target mRNAs, miRNAs mediate gene silencing by either inhibiting translation or promoting mRNA degradation [1–3]. Given their critical involvement in genetic networks and cellular signaling cascades, alterations in miRNA expression play a central role in many scenarios that can trigger the development of pathological processes, including cancer [4–10]. As master regulators of eukaryotic gene expression, tumor-associated miRNAs can be used as biological targets to explore new avenues for development of highly-selective and potent treatments against cancer, which currently suffer from the cytotoxic effects of chemotherapies and radiotherapies, with inevitable side effects and limited success [11,12]. Catalytic targeting of oncogenic miRNA sequences can allow a desirable therapeutic response through fine-tuned regulation of tumor-associated proteins to prevent cancer exacerbation. To date, several advanced technologies have been proposed to effectively attenuate the extreme functionality of miRNAs, such as CRISPR/Cas9 system [13,14], anti-miRNA oligonucleotides [15–23], miRNA sponges [24–29], miRNA zippers [30] and synthetic circular RNAs (circRNAs) [31–33]. Several oligonucleotide-based therapeutics, including miravirsen targeting miR-122 for hepatitis C, are in late-stage clinical trials [34], underscoring the promising potential of miRNA-based treatments.

However, miRNA targeting faces considerable challenges. Unlike messenger RNAs, intracellular miRNAs are shown to have increased rates of production, high intracellular concentrations, as well as extended stability and long-term functioning within protective AGO2 protein environment [35]. Such characteristics intensify even more during pathogenesis and thus require new smart approaches to provide rapid, irreversible and persistent multi-turnover inactivation of emerging miRNA targets in order to overcome the need for multiple or continuous application of high treatment doses. “Smart”, highly-controllable, miRNA-specific supramolecular assemblies offer unique opportunity to achieve that through accurate, effective and continuing knockdown of pathologically-overexpressed miRNAs. To achieve that, we have recently developed biocatalytic conjugates (aRNases) capable to capture the selected RNAs through their recognition oligonucleotide domain and induce selective degradation of the target sequence using covalently attached catalytic groups [36–43]. By considering all stages of the established regulatory mechanism of miRNAs (see below), truly-catalytic and synergistic destruction of often prolific miRNA becomes possible.

According to recently reported data [44], miRNA sequences contain four distinct functional determinants that are crucial for their biological functionality (Fig. 1A). In a cell, a significant proportion of miRNAs is present in the AGO2-bound state, which provides their protection from premature destruction. The 5′- and 3′-ends of miRNA selectively anchor themselves to specific pockets of AGO2 within the MID and PAZ domains, respectively [45–47]. Once mature miRNA is incorporated into AGO2, each nucleotide begins to operate as an element of one of the four functional determinants of miRNA. The principal step of miRNA-mediated post-transcriptional regulation, which is common for any miRNA species, is its binding to the mRNA 3′-untranslated region *via* the seed region (2–7 nts) and 3′-supplementary pairing region (13–16 nts). Next, the miRNA central (8–12 nts) and terminal (17–21/25 nts) regions ensure that the conformational competence is achieved for mRNA repression or degradation [44,45] (Fig. 1A). Although all four functional segments of miRNA play their particular roles in post-transcriptional mRNA repression, the seed region is broadly recognized as a primary determinant for targeting efficacy and sequence-specificity, which controls the selection of mRNA sequences for miRNA-guided repression through RISC-mediated cleavage. For this reason, the seed region is often considered as an important target site for silencing therapeutically significant miRNAs. For example, the recent applications of “tiny” LNA oligonucleotides targeted exclusively to the seed region resulted in effective knockdown of the target miRNAs and led to a pronounced antitumor effect [48,49].

Earlier, we developed several structurally-different variants of aRNases, each able to destroy one or two specific, functionally-significant miRNA determinants [36–39]. Cleavage activity of such aRNases was provided by a short amphiphilic peptide Acetyl-$[LRLRG]_2$-COOH, which contained alternating basic (arginine) and hydrophobic (leucine) amino acids, as well as two glycine residues to enhance the conformational flexibility of the peptide [36,37,39–41]. The hypothetical mechanism of RNA transesterification by this catalytic peptide through synchronized action of two guanidinium groups of arginine residues in catalysis was suggested earlier [40,41]. However, until now, all our previous attempts to selectively demolish the “seed” region of miRNA by catalytic action of aRNases have been unsuccessful [36]. Here, we addressed this challenge through design of novel “Crab”-like conjugates, with a recognition oligonucleotide domain positioned centrally, adjacent to the functional regions of the RNA sequence (Fig. 1A). Two catalytic peptides (“pincers”) were covalently attached at the 5′- and 3′-ends of the recognition motif to attack the functional regions of the captured RNA, and its complementary hybridizing regions, by harnessing the supramolecular dynamics of *RNA-DNA* complexes to drive catalytic turnover. The distinctive feature of these “Crab”-like aRNases is that, by using concurrently two “pincers”, such conjugates can simultaneously attack and cleave miRNA at different sites to produce smaller cleavage products. This would not only compromise the critically significant functional domains of this regulatory molecule (*e.g.*, seed determinant and the 3′-terminal region), but could also facilitate the *rate-limiting* removal of fragmented RNA through hybridization of the new, intact miRNA copy. We investigated biological functionality of this approach by synthesizing a series of “Crab” conjugates against two different oncogenic miRNAs (miR-21 and miR-17). The catalytic performance of “bis”-conjugated “Crab” aRNases (Fig. 1A) was compared to those of the corresponding “single” conjugates (Fig. 1E and G), which carried only one stretch of the peptide located at either 5′- or 3′-end of the recognition oligonucleotide. Mathematical modeling of the hybridized complexes between the target miRNAs and matched “Crabs” illuminated differences in the dynamics of peptide attack within the different heteroduplex complexes that could potentially exist under experimental conditions, thus explaining observed miRNA cleavage patterns. For each of the main supramolecular structural possibility considered here, we analyzed the probability of two arginine guanidinium groups simultaneously approaching each bond in the heteroduplexed target miRNA, which is necessary for their synchronized action as proton shuttles in this molecular catalysis [40]. Simulations were combined with the experimentally-observed cleavage data to estimate the underlying base-sensitivity of cleavage and illuminate the role of supramolecular structural dynamics on catalysis by RNA transesterification. The ability of “Crab” conjugates to recruit RNase H and work with additional synergy against oncogenic miRNA, demonstrated *in vitro*, appears likely to be one of the main factors of their high efficiency here, both in cultured cancer cells and in murine xenograft models, where a single exposure to “Crab” aRNases suppressed their malignant properties and inhibited tumor growth.

2. Materials and methods

2.1. Chemicals and equipment

All chemicals and solvents were purchased from Sigma-Aldrich (UK) unless stated otherwise. Water was purified using a Milli-Q purification system (Millipore, Burlington, USA). UV spectra of oligonucleotides,

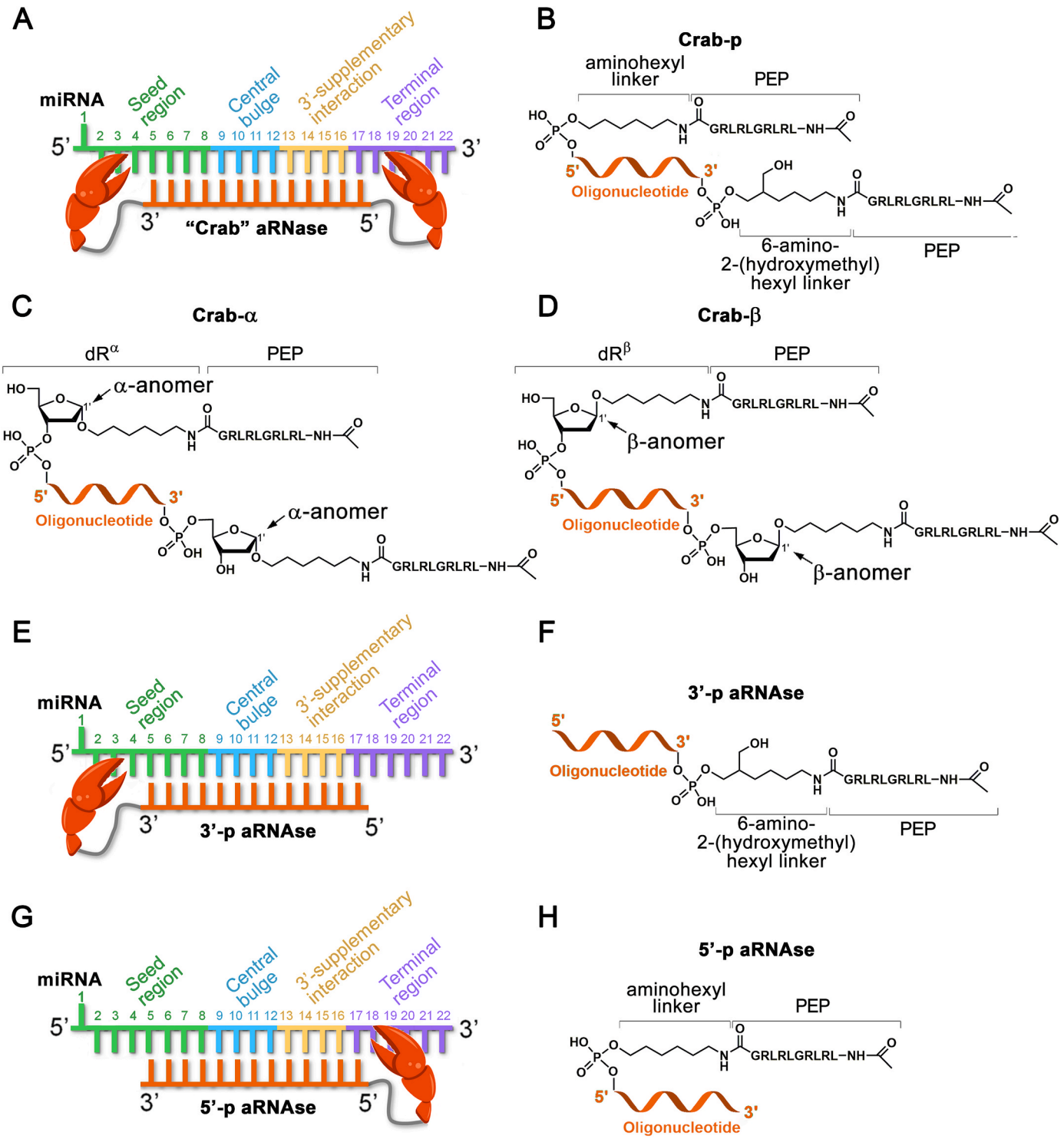

Fig. 1. Schematic illustration of the aRNase systems studied. **(A, E, G)** Design concept of "Crab"-type aRNases (**A**) and "mono" peptidyl-oligonucleotide conjugates (**E** and **G**), showing the recognition motif of the peptidyl-oligonucleotide conjugate (red) hybridizing with the central part of the target miRNA, thus positioning the unhybridized single-stranded 5′-seed region and 3′-terminal region of miRNA for cleavage by catalytic peptide ("crab pincers") located either at the 3′-end (**E**) or 5′-end (**G**) in comparison with the "bis"-conjugated "Crab" aRNase (**A**). **(B-D)** and **(F, H)** Structural features of the peptide attachment points for different representatives of studied aRNases. In the case of Crab-p (**B**) and 3′-p (**F**) or 5′-p (**H**) "mono"-conjugates, catalytic peptides were attached through the 6-amino-2(hydroxymethyl)hexyl linker located at the 3′-phosphate and/or through the aminohexyl linker located at the 5′-phosphate of the recognition motifs. (**C, D**) Crab-α and Crab-β conjugates, where peptides were conjugated to the aminohexyl linkers attached to an anomeric C1′-carbon of the flanking abasic sugar residues either in α- (**C**) or β-configuration (**D**) at 5′- and 3′-termini of oligonucleotide. (For interpretation of the references to colour in this figure legend, the reader is referred to the Web version of this article.)

peptides and peptidyl-oligonucleotide conjugates were recorded on a Varian Cary 4000 dual beam UV–Vis spectrophotometer (Melbourne, Australia). ^{1}H NMR spectra were acquired using Bruker Avance II + spectrometers operating at proton frequencies of 400 MHz using BBI ^{1}H/D-BB Z-GRD Z8202/0347 probe. MALDI (matrix-assisted laser desorption ionization) mass spectra were collected on a Bruker Daltonics Autoflex Speed MALDI-TOF mass spectrometer (MA, USA) at the Centre of Collective Use, Institute of Chemical Biology and Fundamental Medicine (ICBFM SB RAS, Novosibirsk, Russia).

2.2. Oligonucleotide synthesis

Abasic monomers (dR$^{\alpha}$ TFA-amino modifier C6 CE-phosphoramidite and dR$^{\beta}$ TFA-amino modifier C6 CE-phosphoramidite) with an aminohexyl linker attached at the C1′ position in α- or β-configuration were purchased from LINK LGC (Bellshill, Scotland, UK). Oligodeoxyribonucleotides ON-α-21, ON-β-21, ON-α-17 and ON-α-Scr (Table S1) incorporating the flanking abasic nucleotides dR$^{\alpha}$ or dR$^{\beta}$ and carrying aminohexyl linkers at the anomeric carbon C1′ in α- or β-configuration, as well as unmodified oligodeoxyribonucleotides ON-21, ON-17 and ON-Scr (Table S1), were synthesized in the Laboratory of Medicinal Chemistry, Institute of Chemical Biology and Fundamental Medicine (ICBFM SB RAS, Novosibirsk, Russia), according to the standard phosphoramidite protocol in an ASM-800 synthesizer (Biosset, Novosibirsk, Russia) using a solid support, nucleoside phosphoramidites, and a chemical phosphorylation reagent from Glenn Research (Sterling, USA). Oligonucleotides were isolated using consecutive ion-exchange (Polysil SA-500 columns, Russia) and reverse-phase HPLC (LiChrosorb RP-18 columns, Merck, Kenilworth, USA) according to the standard protocols. Oligodeoxyribonucleotides ON-p-21, ON-5′-p-21 and ON-3′-p-21 (Table S1) carrying aminohexyl linker(s) attached at the 5′- and/or 3′-terminal phosphate groups were purchased from ATDBio Ltd (Southampton, UK). Acetyl-[LRLRG]$_2$-CO_2H was purchased from Biomatik (Kitchener, Ontario, Canada). MiRNAs miR-21 and miR-17 were synthesized by Dr. Maria I. Meschaninova (ICBFM SB RAS, Novosibirsk, Russia).

2.3. Conjugate synthesis

The oligonucleotide precursor (0.1 μmol) carrying aminohexyl functional group(s) attached either at the flanking abasic nucleotides (dR$^{\alpha}$ or dR$^{\beta}$), or at the 5′- and/or 3′-terminal phosphates groups was converted from the water-soluble Li^+ form to the DMSO-soluble cetyltrimethylammonium (CTAB) as previously reported in Refs. [40,41]. In order to avoid side reactions detected previously, the earlier reported coupling protocols [40,41] were amended by: (i) reducing the molar excesses of the peptide and 4-dimethylaminopyridine (DMAP) over the oligonucleotide component and (ii) by decreasing the reaction temperature from 60 °C to 40 °C. Acetyl-[LRLRG]$_2$-COOH peptide (3 μmol, 30-fold excess over the oligonucleotide component) was dissolved in anhydrous DMSO (20 μL) and pre-activated by N, N′-dicyclohexylcarbodiimide (DCC) (6.9 μmol, 2.3-fold excess over peptide) and DMAP (3.6 μmol, 1.2 excess over peptide) by adding aliquots (10 μL each) from the freshly-prepared 10-fold stock solutions in anhydrous DMSO. The resulting mixture (40 μL) was then added directly to the oligonucleotide component, and the reaction was left for 24 h at 40 °C. The conjugate, along with unreacted oligonucleotide precursor, was isolated from the reaction mixture using previousely reported protocols [40,41]. In instances where different amounts of the oligonucleotide were used, the concentration of the peptide, DMAP and DCC were re-scaled accordingly to maintain the above molar ratios.

2.4. Conjugate purification and characterization

Prior to HPLC purification, size-exclusion chromatography was used to isolate the oligonucleotide material from the other reagents by employing disposable Illustra NAP-25 columns pre-packed with Sephadex G-25 DNA grade (GE Healthcare Life Sciences). The eluted fractions (2.5 mL) were collected, and their UV–visible spectra were recorded between 210 nm and 500 nm to identify oligonucleotide material.

Peptidyl-oligonucleotide conjugates were further purified by reversed-phase (RP) HPLC using Agilent 1100 (Agilent Technologies, Santa Clara, CA) HPLC system equipped with diode array detector and Rheodyne (3725i) manual injector on a semi-preparative Phenomenex Luna C-18 column (5 μm, 10 × 250 mm, 100 A, Phenomenex; CA, USA). The mobile phase included 0.05 M $LiClO_4$ in water as eluent A and 0.05 M $LiClO_4$ in 100 % acetonitrile as eluent B. After injection, the initial step involved a 3-min run with 100 % A, followed by linear increase of B from 0 % to 40 % over 40 min at flow rate of 2.0 mL/min. The eluted fractions were monitored through continuous collection of UV–visible spectra (210–500 nm) during chromatographic separations, when the oligonucleotide material was identified *via* its characteristic UV absorbance at 260 nm. After lyophilization, each collected conjugate was desalted by size-exclusion chromatography in three consecutive runs using disposable Illustra NAP-25 columns, as described above, to quantitatively remove any residual traces of $LiClO_4$, when their concentrations were evaluated by measuring their UV absorbance at 260 nm and applying their millimolar extinction coefficients ε_{260}. The identity and purity of conjugates were confirmed by RP-HPLC, ^{1}H NMR spectroscopy and mass spectrometry. The analytical data are given in the Supplementary Information (see Figs. S1–S4), while the full characterization of the peptidyl-oligonucleotide conjugates is summarized below.

Crab-α-21 (PEP-dR$^{\alpha}$-ATCAGTCTGATAA-dR$^{\alpha}$-PEP). RP-HPLC fraction was collected at around 31 min (ε_{260} = 134.6 mM^{-1} cm^{-1}, sequestered quantity: 9.08 O.D. at 260 nm, 67.5 nmol). MALDI-MS: m/z = 7016.48 [M + Li], MW = 7010.54 g mol^{-1} calcd. for [$C_{258}H_{404}N_{95}O_{109}P_{14}$]$^-$ (see Fig. S1).

^{1}H NMR (Fig. S2A) (D_2O with TSP (0.01 mM), 400 MHz): δ 0.72–0.80 (m, 48H, Leu-H$^{\delta}$), 0.90–2.95 (m, 128H, 15 × H2′ and 15 × H2″ sugar ring protons, 12H (4 × CH_3 of 4 × dT), 16H of 16 × Arg-H$^{\beta}$, 16H of 16 × Arg-H$^{\gamma}$, 16H of 16 × Leu-H$^{\beta}$, 8H of 8 × Leu-H$^{\gamma}$, 24H of 2 × (6 × CH_2) from 2 × aminohexyl linkers, 6H of 2 × acetyl-CH_3), 3.18 (m, 16H, 16 × Arg-H$^{\delta}$), 3.42–4.40 (m, 69H, 45H of 15 × H4'/H5'/H5" sugar ring protons, 8H of 4 × Gly-CH_2, 16H of 16 × Leu/Arg-H$^{\alpha}$), 5.50–6.35 (m, 17H, 15 × H1' sugar ring protons, 2 × H5 of dC), 7.21–8.41 (m, 18H, 18 × Ar-H from dG(H8 × 2), dA(H8 × 5), dA(H2 × 5), dC(H6 × 2) and dT(H6 × 4)).

Crab-β-21 (PEP-dR$^{\beta}$-ATCAGTCTGATAA-dR$^{\beta}$-PEP). RP-HPLC fraction was collected at 31 min (ε_{260} = 134.6 mM^{-1} cm^{-1}, sequestered quantity: 5.47 O.D. at 260 nm, 40.6 nmol). MALDI-MS: m/z = 7031.95 [M + 3 × Li], MW = 7010.54 g mol^{-1} calcd. for [$C_{258}H_{404}N_{95}O_{109}P_{14}$]$^-$ (Fig. S1).

^{1}H NMR (Fig. S2B) (D_2O with TSP (0.01 mM), 400 MHz): δ 0.72–0.80 (m, 48H, Leu-H$^{\delta}$), 0.90–2.95 (m, 128H, 15 × H2′ and 15 × H2″ sugar ring protons, 12H (4 × CH_3 of 4 × dT), 16H of 16 × Arg-H$^{\beta}$, 16H of 16 × Arg-H$^{\gamma}$, 16H of 16 × Leu-H$^{\beta}$, 8H of 8 × Leu-H$^{\gamma}$, 24H of 2 × (6 × CH_2) from 2 × aminohexyl linkers, 6H of 2 × acetyl-CH_3), 3.18 (m, 16H, 16 × Arg-H$^{\delta}$), 3.42–4.40 (m, 69H, 45H of 15 × H4'/H5'/H5" sugar ring protons, 8H of 4 × Gly-CH_2, 16H of 16 × Leu/Arg-H$^{\alpha}$), 5.50–6.35 (m, 17H, 15 × H1' sugar ring protons, 2 × H5 of dC), 7.21–8.41 (m, 18H, 18 × Ar-H from dG(H8 × 2), dA(H8 × 5), dA(H2 × 5), dC(H6 × 2) and dT(H6 × 4)).

Crab-p-21 (PEP–NH–$(CH_2)_6$-p-ATCAGTCTGATAA-p–CH_2–CH(CH_2OH)-$(CH_2)_4$-NH-PEP). RP-HPLC fraction was collected at around 29 min (ε_{260} = 134.6 mM^{-1} cm^{-1}, final quantity: 3.74 O.D. at 260 nm, 27.8 nmol) MALDI-MS: m/z = 6829.33 [M + 3 × Li], MW = 6809.46 g mol^{-1} calcd. for [$C_{249}H_{391}N_{95}O_{104}P_{14}$] (Fig. S1).

^{1}H NMR (Fig. S2C) (D_2O with TSP (0.01 mM), 400 MHz): δ 0.72–0.80 (m, 48H, Leu-H$^{\delta}$), 0.90–2.95 (m, 125H, 13 × H2′ and 13 × H2″ sugar ring protons, 12H (4 × CH_3 of 4 × dT), 16H of 16 × Arg-H$^{\beta}$, 16H of 16 × Arg-H$^{\gamma}$, 16H of 16 × Leu-H$^{\beta}$, 8H of 8 × Leu-H$^{\gamma}$, 12H of 6 × CH_2 from 5′-aminohexyl linker, 13H from 3′-6-amino-2-(hydroxymethyl)hexyl linker, 6H of 2 × acetyl-CH_3), 3.18 (m, 16H, 16 × Arg-H$^{\delta}$), 3.42–4.40 (m, 69H, 39H of 13 × H4'/H5'/H5″ sugar ring protons, 8H of 4 × Gly-CH_2, 16H of 16 × Leu/Arg-H$^{\alpha}$), 5.50–6.35 (m, 15H, 13 × H1′ sugar ring

protons, 2 × H5 of dC), 7.21–8.41 (m, 18H, 18 × Ar-H from dG(H8 × 2), dA(H8 × 5), dA(H2 × 5), dC(H6 × 2) and dT(H6 × 4)).

Crab-α-17 (PEP-dR$^{\alpha}$-TGCACTGTAAGCA-dR$^{\alpha}$-PEP). RP-HPLC fraction was collected at around 31 min (ε_{260} = 123.3 mM^{-1} cm^{-1}, final quantity: 2.4 O.D. at 260 nm, 19.6 nmol). MALDI-MS: *m/z* = 7028.35 [M + 2 × Li + 2 × H)], MW = 7012.53 g mol^{-1} calcd. for [$C_{257}H_{404}N_{96}O_{109}P_{14}$] (Fig. S1).

^{1}H NMR (Fig. S3A) (D_2O with TSP (0.01 mM), 400 MHz): δ 0.72–0.80 (m, 48H, Leu- H$^{\delta}$), 0.90–2.95 (m, 125H, 15 × H2′ and 15 × H2″ sugar ring protons, 9H (3 × CH_3 of 3 × dT), 16H of 16 × Arg-H$^{\beta}$, 16H of 16 × Arg-H$^{\gamma}$, 16H of 16 × Leu-H$^{\beta}$, 8H of 8 × Leu-H$^{\gamma}$, 24H of 2 × (6 × CH_2) from 2 × aminohexyl linkers, 6H of 2 × acetyl-CH_3), 3.18 (m, 16H, 16 × Arg-H$^{\delta}$), 3.42–4.40 (m, 69H, 45H of 15 × H4'/H5'/H5" sugar ring protons, 8H of 4 × Gly-CH_2, 16H of 16 × Leu/Arg-H$^{\alpha}$), 5.50–6.35 (m, 18H, 15 × H1' sugar ring protons, 3 × H5 of dC), 7.21–8.41 (m, 17H, 17 × Ar-H from dG(H8 × 3), dA(H8 × 4), dA(H2 × 4), dC(H6 × 3) and dT (H6 × 3)).

Crab-α-Scr (PEP-dR$^{\alpha}$-CAAGTCTCGTATG-dR$^{\alpha}$-PEP). RP-HPLC fraction was collected at around 31 min (ε_{260} = 123.9 mM^{-1} cm^{-1}, final quantity: 7.84 O.D. at 260 nm, 63.3 nmol). MALDI-MS: *m/z* = 7017.82 [M + 2 × Li], MW = 7003.52 g mol^{-1} calcd. for [$C_{257}H_{405}N_{93}O_{111}P_{14}$] (Fig. S1).

^{1}H NMR (Fig. S3B) (D_2O with TSP (0.01 mM), 400 MHz): δ 0.72–0.80 (m, 48H, Leu- H$^{\delta}$), 0.90–2.95 (m, 128H, 15 × H2′ and 15 × H2″ sugar ring protons, 12H (4 × CH_3 of 4 × dT), 16H of 16 × Arg-H$^{\beta}$, 16H of 16 × Arg-H$^{\gamma}$, 16H of 16 × Leu-H$^{\beta}$, 8H of 8 × Leu-H$^{\gamma}$, 24H of 2 × (6 × CH_2) from 2 × aminohexyl linkers, 6H of 2 × acetyl-CH_3), 3.18 (m, 16H, 16 × Arg-H$^{\delta}$), 3.42–4.40 (m, 69H, 45H of 15 × H4'/H5'/H5" sugar ring protons, 8H of 4 × Gly-CH_2, 16H of 16 × Leu/Arg-H$^{\alpha}$), 5.50–6.35 (m, 18H, 15 × H1' sugar ring protons, 3 × H5 of 3 × dC), 7.21–8.41 (m, 16H, 16 × Ar-H from dG(H8 × 3), dA(H8 × 3), dA(H2 × 3), dC(H6 × 3) and dT(H6 × 4)).

5′-p-21 (PEP–NH–$(CH_2)_6$-p-ATCAGTCTGATAA). RP-HPLC fraction was collected at around 24 min (ε_{260} = 134.6 mM^{-1} cm^{-1}, final quantity: 10.58 O.D. at 260 nm, 78.6 nmol). MALDI-MS: *m/z* = 5401.37 [M-H + 5 × Li], MW = 5367.58 g mol^{-1} calcd. for [$C_{188}H_{275}N_{72}O_{89}P_{13}$] (see Fig. S1).

^{1}H NMR (Fig. S4A) (D_2O with TSP (0.01 mM), 400 MHz): δ 0.72–0.80 (m, 24H, Leu-H$^{\delta}$), 0.90–2.95 (m, 81H, 13 × H2′ and 13 × H2″ sugar ring protons, 12H (4 × CH_3 of 4 × dT), 8H of 8 × Arg-H$^{\beta}$, 8H of 8 × Arg-H$^{\gamma}$, 8H of 8 × Leu-H$^{\beta}$, 4H of 4 × Leu-H$^{\gamma}$, 12H of 6 × CH_2 from aminohexyl linker, 3H of acetyl-CH_3), 3.18 (m, 16H, 16 × Arg-H$^{\delta}$), 3.42–4.40 (m, 51H, 39H of 13 × H4'/H5'/H5" sugar ring protons, 4H of 2 × Gly-CH_2, 8H of 8 × Leu/Arg-H$^{\alpha}$), 5.50–6.35 (m, 15H, 13 × H1' sugar ring protons, 2 × H5 of dC), 7.21–8.41 (m, 18H, 18 × Ar-H from dG(H8 × 2), dA(H8 × 5), dA(H2 × 5), dC(H6 × 2) and dT(H6 × 4)).

3′-p-21 (ATCAGTCTGATAA-p–CH_2–CH(CH_2OH)–$(CH_2)_4$–NH-PEP). RP-HPLC fraction was collected at around 24 min (ε_{260} = 134.6 mM^{-1} cm^{-1}, final quantity: 7.30 O.D. at 260 nm, 54.2 nmol). MALDI-MS: *m/z* = 5399.60 [M + 2H], MW = 5397.59 g mol^{-1} calcd. for [$C_{189}H_{277}N_{72}O_{90}P_{13}$] (see Fig. S1).

^{1}H NMR (Fig. S4B) (D_2O with TSP (0.01 mM), 400 MHz): δ 0.72–0.80 (m, 24H, Leu-H$^{\delta}$), 0.90–2.95 (m, 82H, 13 × H2′ and 13 × H2″ sugar ring protons, 12H (4 × CH_3 of 4 × dT), 8H of 8 × Arg-H$^{\beta}$, 8H of 8 × Arg-H$^{\gamma}$, 8H of 8 × Leu-H$^{\beta}$, 4H of 4 × Leu-H$^{\gamma}$, 13H from 13H from 3′-6-amino-2-(hydroxymethyl)hexyl linker, 3H of acetyl-CH_3), 3.18 (m, 16H, 16 × Arg-H$^{\delta}$), 3.42–4.40 (m, 51H, 39H of 13 × H4'/H5'/H5″ sugar ring protons, 4H of 2 × Gly-CH_2, 8H of 8 × Leu/Arg-H$^{\alpha}$), 5.50–6.35 (m, 15H, 13 × H1′ sugar ring protons, 2 × H5 of dC), 7.21–8.41 (m, 18H, 18 × Ar-H from dG(H8 × 2), dA(H8 × 5), dA(H2 × 5), dC(H6 × 2) and dT(H6 × 4)).

5′-α-21/3′-α-21 (PEP-dR$^{\alpha}$-ATCAGTCTGATAA-dR$^{\alpha}$ and dR$^{\alpha}$-ATCAGTCTGATAA-dR$^{\alpha}$-PEP). RP-HPLC fraction was collected at around 26 min as reaction by-product (ε_{260} = 134.6 mM^{-1} cm^{-1}, final quantity: 9.0 O.D. at 260 nm, 66.9 nmol). ^{1}H NMR (Fig. S4C) (D_2O with TSP (0.01 mM), 400 MHz): δ 0.72–0.80 (m, 24H, Leu-H$^{\delta}$), 0.90–2.95 (m, 85H, 15 × H2′ and 15 × H2″ sugar ring protons, 12H (4 × CH_3 of 4 × dT), 8H of 8 × Arg-H$^{\beta}$, 8H of 8 × Arg-H$^{\gamma}$, 8H of 8 × Leu-H$^{\beta}$, 4H of 4 × Leu-H$^{\gamma}$, 24H of 2 × (6 × CH_2) from two aminohexyl linkers, 3H of acetyl-CH_3), 3.18 (m, 16H, 16 × Arg-H$^{\delta}$), 3.42–4.40 (m, 69H, 45H of 15 × H4'/H5'/H5″ sugar ring protons, 8H of 4 × Gly-CH_2, 16H of 16 × Leu/Arg-H$^{\alpha}$), 5.50–6.35 (m, 17H, 15 × H1′ sugar ring protons, 2 × H5 of dC), 7.21–8.41 (m, 18H, 18 × Ar-H from dG(H8 × 2), dA(H8 × 5), dA(H2 × 5), dC(H6 × 2) and dT(H6 × 4)).

5′-α-17/3′-α-17 (PEP-dR$^{\alpha}$-TGCACTGTAAGCA-dR$^{\alpha}$ and dR$^{\alpha}$-TGCACTGTAGCA-dR$^{\alpha}$-PEP) RP-HPLC fraction was collected at around 27 min as reaction by-product (ε_{260} = 123.3 mM^{-1} cm^{-1}, final quantity: 3.192 O.D. at 260 nm, 26.0 nmol). ^{1}H NMR (Fig. S4D) (D_2O with TSP (0.01 mM), 400 MHz): δ 0.72–0.80 (m, 24H, Leu- H$^{\delta}$), 0.90–2.95 (m, 82H, 15 × H2′ and 15 × H2″ sugar ring protons, 9H (3 × CH_3 of 3 × dT), 8H of 8 × Arg-H$^{\beta}$, 8H of 8 × Arg-H$^{\gamma}$, 8H of 8 × Leu-H$^{\beta}$, 4H of 4 × Leu-H$^{\gamma}$, 24H of 2 × (6 × CH_2) from two aminohexyl linkers, 3H of acetyl-CH_3), 3.18 (m, 8H, 8 × Arg-H$^{\delta}$), 3.42–4.40 (m, 57H, 45H of 15 × H4'/H5'/H5″ sugar ring protons, 4H of 2 × Gly-CH_2, 8H of 8 × Leu/Arg-H$^{\alpha}$), 5.50–6.35 (m, 18H, 15 × H1′ sugar ring protons, 3 × H5 of 3 × dC), 7.21–8.41 (m, 17H, 17 × Ar-H from dG(H8 × 3), dA(H8 × 4), dA(H2 × 4), dC(H6 × 3) and dT(H6 × 3)).

5′-α-Scr/3′-α-Scr (PEP-dR$^{\alpha}$-CAAGTCTCGTATG-dR$^{\alpha}$ and dR$^{\alpha}$-CAAGTCTCGTATG-dR$^{\alpha}$-PEP). RP-HPLC fraction was collected at around 27 min as reaction by-product (e_{260} = 123.9 mM^{-1} cm^{-1}, final quantity: 12.38 O.D. at 260 nm, 99.9 nmol). ^{1}H NMR (Fig. S3C) (D_2O with TSP (0.01 mM), 400 MHz): δ 0.72–0.80 (m, 24H, Leu- H$^{\delta}$), 0.90–2.95 (m, 97H, 15 × H2′ and 15 × H2″ sugar ring protons, 12H (4 × CH_3 of 4 × dT), 8H of 8 × Arg-H$^{\beta}$, 8H of 8 × Arg-H$^{\gamma}$, 8H of 8 × Leu-H$^{\beta}$, 4H of 4 × Leu-H$^{\gamma}$, 24H of 2 × (6 × CH_2) from two aminohexyl linkers, 3H of acetyl-CH_3), 3.18 (m, 8H, 8 × Arg-H$^{\delta}$), 3.42–4.40 (m, 57H, 45H of 15 × H4'/H5'/H5″ sugar ring protons, 4H of 2 × Gly-CH_2, 8H of 8 × Leu/Arg-H$^{\alpha}$), 5.50–6.35 (m, 18H, 15 × H1′ sugar ring protons, 3 × H5 of 3 × dC), 7.21–8.41 (m, 16H, 16 × Ar-H from dG(H8 × 3), dA(H8 × 3), dA(H2 × 3), dC(H6 × 3) and dT(H6 × 4)).

In the above ^{1}H NMR spectra, H3' sugar ring protons (4.3–5.2 ppm) were not analyzed due to suppression of the residual water signal at 4.76 ppm.

2.5. Cy5.5 labeling of conjugates

The introduction of the Cy5.5 tag into the conjugate was carried out in the reaction of Cy5.5 N-Hydroxy-succinimide (NHS) ester (Lumiprobe, Russian Federation) with a free amino group of 5′-α-Scr/3′-α-Scr conjugate (Fig. S3C, Fig. S5, Table 1). The reaction was carried out in 100 μL of 100 mM HEPES buffer, pH 8.3, containing 200 μM aqueous solution of conjugate and a 20-fold molar excess of Cy5.5 NHS ester, freshly dissolved in DMSO. The mixture was incubated for 20 h at room temperature with constant shaking. Subsequently, the separation of the labeled conjugate was achieved by precipitation with 1 mL of 2 % $LiClO_4$ in acetone at −80 °C overnight, while the unreacted Cy5.5 ester remained dissolved in the organic phase. The Cy5.5-labeled 5′-α-Scr/3′-α-Scr conjugate was then isolated by centrifugation at 14,000 rpm for 20 min, followed by four washes with acetone. After air-drying, the conjugate was dissolved in sterile water and stored at −20 °C for further application.

2.6. RNA labelling

5′-end labelling using [^{32}P]–ATP and T4 polynucleotide kinase (ThermoScientific, Waltham, USA) and the isolation of synthetic single-stranded [P^{32}]-miRNAs miR-21 5′ UAGCUUAUCAGACUGAUGUUGA-3′ and miR-17 5′-CAAAGUGCUUACAGUGCAGGUAG-3′ were carried out according to the procedure described previously [50,51].

Table 1
Peptidyl-oligonucleotide conjugates used in the study.

Nomenclature	Sequence 5′→3′	k_{obs}, × 10^{-6}, s^{-1}
Anti-miR-21		
Crab-α-21	PEP-dR^{α}-ATCAGTCTGATAA-dR^{α}-PEP	4.50 ± 0.56(1) 2.56 ± 0.10(2)
Crab-β-21	PEP-dR^{β}-ATCAGTCTGATAA-dR^{β}-PEP	6.07 ± 0.29(1) 4.64 ± 0.12(2)
Crab-p-21	PEP–NH–$(CH_2)_6$-p-ATCAGTCTGATAA-p–CH_2–$CH(CH_2OH)$–$(CH_2)_4$–NH-PEP	20.08 ± 1.73(1) 22.34 ± 2.92(2)
5′-p-21	PEP–NH–$(CH_2)_6$-p-ATCAGTCTGATAA	0.61 ± 0.05(1) ND(2)
3′-p-21	ATCAGTCTGATAA-p–CH_2–$CH(CH_2OH)$–$(CH_2)_4$–NH-PEP	1.91 ± 0.02(1) ND(2)
5′-α-21/3′-α-21*	PEP-dR^{α}-ATCAGTCTGATAA-dR^{α} and dR^{α}-ATCAGTCTGATAA-dR^{α}-PEP	0.67 ± 0.04(1) ND(2)
Anti-miR-17		
Crab-α-17	PEP-dR^{α}-TGCACTGTAAGCA-dR^{α}-PEP	88.55 ± 4.43(1) 49.08 ± 7.01(2)
5′-α-17/3′-α-17*	PEP-dR^{α}-TGCACTGTAAGCA-dR^{α} and dR^{α}-TGCACTGTAAGCA-dR^{α}-PEP	3.17 ± 0.36(1) ND(2)
Scrambled non targeted		
Crab-α-Scr	PEP-dR^{α}-CAAGTCTCGTATG-dR^{α}-PEP	1.75 ± 0.19(3) 1.02 ± 0.04(4) ND(2)
5′-α-Scr/3′-α-Scr*	PEP-dR^{α}-CAAGTCTCGTATG-dR^{α} and dR^{α}-CAAGTCTCGTATG-dR^{α}-PEP	ND

Where: PEP – catalytic peptide $[LRLRG]_2$-CO_2H, dR^{α} and dR^{β} – abasic nucleotide with aminohexyl linker attached to the anomeric C1′ carbon in α or β configuration (see also Fig. 1C and D). The aminohexyl linker and 3′-6-amino-2-(hydroxymethyl)hexyl linker attached to the 5′- and 3′-phosphate group of the recognition oligonucleotide, respectively, is indicated here as –NH–$(CH_2)_6$-p- and -p–CH_2–$CH(CH_2OH)$–$(CH_2)_4$–NH- groups (see also Fig. 1B). * by-product of synthesis, which was a mixture of two mono peptidyl-oligonucleotide conjugates (see also Fig. S5). k_{obs} –observed rate constants. (1) single turnover reaction mode ([miRNA] = 1 μM and [aRNase] = 5 μM); (2) multiple turnover reaction mode ([miRNA] = 10 μM and [aRNase] = 5 μM). (3) [miR-21] = 1 μM and [Scr aRNase] = 5 μM. (4) [miR-17] = 1 μM and [Scr aRNase] = 5 μM. ND – not determined. Reactions were performed in Buffer (1).

2.7. Gel-retardation assay

The assay was carried out in Buffer (1) (50 mM Tris-HCl, pH 7.0, 200 mM KCl and 1 mM EDTA) as described previously [39].

2.8. Ribonuclease activity assay

Ribonuclease activity of synthesized aRNases was studied under two conditions: (1) in excess conjugate over miRNA (*single-turnover* reaction mode) and (2) in excess miRNA over conjugate (*multiple turnover* reaction mode). In single turnover experiments, the reaction mixture (10 μL) contained 400 cpm (Cherenkov's counting) of [^{32}P]-miRNA, 1 μM unlabeled miRNA, one of the "Crab" aRNases at a concentration 5 μM and Buffer (1). For multi-turnover experiments, the reaction mixture (14 μL) contained 560 cpm (Cherenkov's counting) of [^{32}P]-miRNA, 10 μM unlabeled miRNA, one of the "Crab" aRNases at a concentration 5 μM and Buffer (1). The mixtures were incubated at 37 °C for 72 h. Sample collection and further data analysis were carried out according to the protocol described earlier in Ref. [36].

The observed rate constants k_{obs} of conjugate-mediated miRNA cleavage were calculated using the following equation:

$$F(t) = \alpha \times \left(1 - e^{-k_{obs} \cdot t}\right) \quad (2)$$

where α is the maximum cleavage, *t* is time, and *F(t)* is the fraction of the substrate cleaved at time t. Half-life miRNA cleavage for each of the aRNase were estimated as follows:

$$\tau_{1/2} = \ln 2 / k_{obs} \quad (3)$$

2.9. Simulation of miRNA cleavage into fragments by aRNases

Watson-Crick base-paired heteroduplexes between each miRNA target and each peptidyl-oligonucleotide aRNase design, comprising peptides conjugated to antisense oligonucleotide were each constructed and assembled in 3D graphics space in Mathematica 13.2 (Wolfram Research Europe Ltd., www.wolfram.com/mathematica/), using established A-form of *RNA-DNA* double-helix parameters, providing 11 base pairs per turn. Our purpose was to interrogate our experimental cleavage data by exploring the accessibility of each phosphodiester bond of the RNA strand(s) in each heteroduplex complex to attack by arginine residues. Consequently, only the locations of each bond and each arginine residue needed to be considered, which allowed the model to consider the whole heteroduplex complex, at this supra-molecular size scale, beyond the scale of Molecular Dynamic modeling reported earlier [40]. We emphasize that the images and animations using 3D graphics are not intended to be molecular models, but instead, only visualization of each heteroduplex complex in the same 3D space used by this coarse model of the relative locations of bonds and arginine residues.

Three different heteroduplex complexes were constructed to include: (i) one miRNA molecule and one conjugate molecule (1:1), (ii) two miRNA molecules and one conjugate molecule (2:1), and (iii) one miRNA molecule and two conjugate molecules (1:2). This allowed the same bond in each RNA target to be considered in three different settings of attack by the peptides: (i) at its location in the 1:1 heteroduplex, also present in (ii) the 2:1 complex plus at its additional location in one of the dangling single strands in, and (iii) in the 1:2 complex where its location in the 1:1 complex relative to the additional peptides conjugated to the dangling strands of the conjugates. Dynamic mixtures of these complexes may be expected in the experimental cleavage studies, namely: with RNA in excess over conjugate, decline in 2:1 heteroduplexing as RNA is cleaved; and with conjugate in excess over RNA, increase in 1:2 heteroduplexing. The likely smaller contributions of other possible complexes were not considered at this stage (*e.g.,* heteroduplexes with cleaved fragments, hairpin loops within each oligonucleotide).

Each conjugated peptide chain was provided with independent pseudorandom motion in the 3D space occupied by these complexes (2:1, 1:1 and 1:2), when the distance between each bond location and each arginine (R) residue in both peptide chains was recorded for each complex for at least 200 peptide motions, which provided the raw data matrix for further analysis. Collision of an arginine residue (R) with the 3D space set around each bond was recorded as a 'Hit'. Simultaneous collisions of two arginine residues in line, across the same bond was recorded as a 'R-R Hit' or probable R-R attack of the bond and a possible cleavage event, based upon earlier Molecular Dynamics modeling [40]. Cleavage was considered only for R-R attack of single-stranded RNA, namely: the non-complementary overhangs at the 3′- and 5′-ends of the 1:1, 2:1 and 1:2 complexes, the additional longer single strands including complementary nucleotides in the 2:1 complexes, and for the edge fraying of the double-stranded regions. Edge fraying was modelled by periodically shifting the positions of the 5 bonds between the 6 nucleotides at each end of the duplex. Where strands competed for binding, 2:1 and 1:2 complexes were also considered in their static and dynamic state of zipping and unzipping of the pair of competing strands (RNA in

the 2:1 or antisense DNA in the 1:2 complexes), by pseudorandom movement of the branch point of their dangling single strands along each heteroduplex.

Our premise was that the probability of R-R attack of each bond and the 'specificity' or likelihood of cleavage of each bond between nucleotide base neighbors along the RNA sequence when attacked are likely the main factors influencing the cleavage observed experimentally. However, this 'specificity' information is buried within experimental cleavage patterns, hidden particularly by the dynamic changes in the availability of the same bond to R-R attack in its multiple structural locations within the dynamic heteroduplex complexes (2:1, 1:1, 1:2). The cleavage patterns observed experimentally were investigated as the product of the probability of attack of each location of the same bond (from the frequency of in-line R-R hits detected for each of its locations in the complexes) and the probability of cleavage of each bond when attacked (the 'specificity' considered here). The R-R attack probabilities only considered complexes with intact RNA target, and not complexes with RNA fragments from earlier cleavage. The effects of additional subsequent complexes with labeled and unlabeled fragments from 'first-cuts' of the RNA were not considered. Consequently, 'specificity' estimated later in the cleavage reactions deviated from the more accurate initial estimates of specificity, which were extracted from experimental cleavage patterns, predominantly resulting from 'first-cuts' of intact RNA molecules into 2 fragments. Further details can be found in Section 1 of Supplementary Information (pages 4–18, including computations).

2.10. Ribonuclease activity assay in the presence of RNase H

The reaction mixture (26 μL) containing 1040 cpm (Cherenkov's counting) of [^{32}P]-miRNA, 10 μM unlabeled miRNA, 5 μM either of an aRNase or an oligonucleotide in Buffer (2) (20 mM Tris-HCl, pH 7.8, 40 mM KCl, 8 mM $MgCl_2$ and 1 mM DTT, ThermoScientific, Waltham, USA) was incubated at 37 °C to form heteroduplexes. After 20 min, RNase H (ThermoScientific, Waltham, USA) was added to a final concentration of 5 U/mL. The mixtures were further incubated at 37 °C for 48 h. Aliquots (2 μL) were taken periodically, when the reaction was quenched, and the RNA cleavage products were collected and analyzed as described above [36].

2.11. Nuclease stability assay

Crab-α-Scr conjugate or peptide-lacking oligonucleotide (0.1 μg/μL) were incubated at 37 °C in Dulbecco's Modified Eagle Medium (DMEM) (Sigma, USA) with 10 % fetal bovine serum (FBS; GE Healthcare, USA) for 72 h. After 0, 0.5, 1, 2, 4, 8, 24, 48 and 72 h aliquots (10 μL) were taken, reaction was quenched by adding equal volume of 8M urea and immediate freezing in liquid nitrogen. Analysis of thawed samples was conducted in 18 % PAAG/8 M urea gels, using Tris-Borate-EDTA (TBE) as running buffer. The gels were stained with Stains-All (MP Biomedicals, USA) and photographed using Versa-Doc 4000 MP Imaging system (Bio-Rad, USA).

2.12. Cell cultures

Murine melanoma B16 cells were obtained from the Cell Culture Bank of the Blokhin National Medical Oncology Research Centre (Moscow, Russia). Human lung carcinoma A-549 cells and human breast adenocarcinoma MCF-7 cells were purchased from the bank of cell cultures of the Institute of Cytology, Russian Academy of Sciences (St. Petersburg, Russia). Non-malignant fibroblasts hFF3 cells were kindly provided by Dr. O. A. Koval, Institute of Chemical Biology and Fundamental Medicine, SB RAS (Novosibirsk, Russian Federation). Cells were cultivated in DMEM supplemented with 10 % FBS and 1 % antibiotic antimycotic solution (10,000 mg/mL streptomycin, 10,000 IU/mL penicillin, and 25 μg/mL amphotericin) (ICN, Germany) at 37 °C in a humidified incubator with 5 % CO_2 (standard conditions).

2.13. Transfection of tumor cells with "Crab" aRNases

Cells were pre-seeded in DMEM containing 10 % FBS a day before transfection and were incubated under standard conditions. Immediately before transfection, the medium was replaced with serum-free DMEM. Transfection was performed by incubation of cells with 1 μM aRNase precomplexed with Lipofectamine™ 2000 (Invitrogen, Waltham, MA, USA) in Opti-MEM medium (Invitrogen, Waltham, MA, USA), according to the manufacturer's guidelines. Four hours after transfection, the medium was replaced by culture medium supplemented with 10 % FBS and 1 % antibiotic antimycotic solution, and the cells were cultivated for 24–96 h under standard conditions.

2.14. Flow cytometry

Four hours after transfection with Cy5.5-labeled conjugate 5′-α-Scr/3′-α-Scr, cells were harvested, washed with saline solution, resuspended and fixed in 4 % formaldehyde in PBS. Cells were analyzed using Novocyte 3000 (ACEA Biosciences, USA) flow cytometer (the excitation wavelength was 640 nm, and the emission wavelength was 675 ± 30 nm). Two parameters reflecting the efficiency of the process were used for the comparison: (1) the transfection efficiency estimated as the percentage of cells with red fluorescence exceeding the maximum level of the auto-fluorescence of untreated cells, and (2) the mean fluorescence intensity of cells measured in relative fluorescent units ('RFU').

2.15. qPCR

After transfection of MCF-7 cells as described above, total RNA was extracted from the cells after periods of 24, 48 and 72 h using TRIzol Reagent (Invitrogen, Waltham, USA), according to the manufacturer's protocol. The levels of miRNAs were measured using stem-loop qPCR approach [52,53] as described previously [17]. The sequences of RT and PCR primers used in the study are listed in Table S2.

2.16. Western-blotting

Cell lysates were prepared in a radioimmunoprecipitation assay (RIPA) buffer (Thermo Scientific, Waltham, USA) 72 h after transfection of MCF-7 cells with "Crab" aRNases as described in Section 2.13. Cell lysates were separated in 12.5 % sodium dodecyl sulfate (SDS)/PAGE and transferred to a poly(vinylidene difluoride) (PVDF) membrane using Criterion™ Blotter (Bio-Rad, USA). The membranes were blocked for 1 h at room temperature in 5 % nonfat dried milk in TBST (20 mM Tris-HCl, pH 7.6, 137 mM NaCl, 0.1 % Tween), and incubated with primary antibodies against PDCD4 (ARG42238, Arigobio, Taiwan, ROC; 1:800), E2F1 (ARG59557, Arigobio, Taiwan, ROC; 1:400), E-cadherin (AF0131, Affinity Biosciences, Cincinnati, OH, USA; 1:1000) and GAPDH (ARG65680, Arigobio, Taiwan, ROC; 1:10000) at 4 °C for 16 h. After three washes with TBST, membranes were incubated with secondary HRP-conjugated goat anti-rabbit antibodies (ab6721, Abcam, UK) at room temperature for 1 h. After three washes with TBST, proteins detection was performed by Versadoc 4000 MP (Bio-Rad, USA) using Chemiluminescent reagent kit (Abcam, USA). Data were analyzed using GelAnalyzer 23.1.1 software (www.gelanalyzer.com).

2.17. WST assay

B16, MCF-7, A-549, hFF3 cells were seeded in 96-well plates at a density of 5 × 10^3 cells per well, transfected with "Crab" aRNases and incubated for 72 h under standard conditions. WST-1 cell proliferation reagent (Roche, Basel, Switzerland) was then added to each well (at 0.1 × volume of culture medium). B16 and A-549 cells were incubated for 1 h, MCF-7 and hFF3 cells for 2 h at 37 °C, when absorbance was determined at 450 and 620 nm with a Multiscan FC (Thermo Scientific, Waltman, USA). Cell viability was estimated by comparing the

absorbance values of the samples after background subtraction.

2.18. xCelligence real-time analysis of cell proliferation and viability

Viability and proliferation of MCF-7 and A-549 cells were measured using an xCelligence real-time cell analysis (RTCA) system (ACEA Biosciences, Santa Clara, USA) for 96 h as described previously [36].

2.19. Mice

10–12 week-old nude mice were kept under 12/12 h light/dark cycle (9–12 a.m., 1–9 pm – light; 9–12 p.m., 1–9 am – darkness) and regulated automatically on a standard diet for laboratory animals (GOST (State Standard) R 5025892) in compliance with the international recommendations of the European Convention for the Protection of vertebrate animals used for experimental studies (1997), as well as the rules of laboratory practice in the performance of preclinical studies in the Russian State Standards (R 51000.3–96 and 51000.4–96). The experimental protocol was approved by the Committee on the Ethics of Animal Experiments of the Institute of Cytology and Genetics of the Siberian Branch of the Russian Academy of Sciences (protocol No. 111 from December 07, 2021).

2.20. Antitumor studies

In order to investigate the antitumor effect of "Crab" aRNases, four different groups of MCF-7 cells were prepared *in vitro*: (1) cells without treatment; (2) cells transfected with control non-targeted Crab-α-Scr; (3) cells transfected with Crab-p-21; and (4) cells transfected with Crab-α-21. Transfection was performed using Lipofectamine™ 2000 with an aRNase concentration of 1 μM, as described in section 2.13. Four hours after transfection, the culture medium was removed, cells were washed and diluted in saline buffer for further implantation into nude mice. Transplantation was performed by subcutaneous injection of MCF-7 cells (10^6 cells in 0.1 mL in sterile saline buffer) into the left flank ($n = 7$ per group). As soon as tumors began to be palpable, the tumor volumes were measured every 2–3 days using calipers. Tumor volumes were calculated as $V = (D \times d^2)/2$, where D is the longest diameter of the tumor node and *d* is the shortest diameter of the tumor node perpendicular to *D*. At day 19, the mice were euthanized, and tumors were collected for further histological analysis.

2.21. Histology and immunohistochemistry

Histological analysis of tumor specimens and immunohistochemical study of the tumor with anti-Ki-67 (ab16667, Abcam, Cambridge, MA, USA) and anti-caspase-3 (ab2302, Abcam, USA) primary antibodies, was carried out as previously reported protocol [17]. All the images were examined and scanned using an Axiostar Plus microscope equipped with an Axiocam MRc5 digital camera (Zeiss, Oberkochen, Germany), operating at × 400 magnification. Morphometric analysis of tumor sections was performed using a counting grid consisting of 100 testing points in a testing area equal to 3.2×10^6 μm^2 and included evaluation of the numerical density (Nv) of mitoses and caspase-3-positive cells, as well as the volume density (Vv, %) of Ki-67-positive cells. At least five random fields, from the tumor specimens of seven mice in each group (total of 35 testing fields) were studied.

2.22. Statistical analysis

Biological data were analyzed using two-tailed unpaired Student's t-tests or one-way ANOVA, followed by Tukey's multiple comparisons test, using GraphPad Prism version 8.4.3 for Windows (GraphPad Software, California, USA). Statistical significance was considered for $p < 0.05$.

3. Results

3.1. Design of peptidyl-oligonucleotides as dynamic supramolecular aRNases

Earlier studies with antisense oligonucleotides armed with cleaving agents produced sequence-specific cleavage of single-stranded regions [42], but lacked the catalytic turnover of an enzyme because the thermodynamic stability of the double-stranded region remained intact, thus restricting turnover to slow exchange between cleaved and intact RNA. Limited turnover was later achieved by cleaving single-stranded regions in bulge-loops induced in the middle of the hybridized RNA, thus leaving a pair of double-stranded regions, with increased turnover [39,41]. An additional pair of dynamic edges at the cleaved bulge regions presumably increased the rate of exchange kinetics. Here, we develop novel peptidyl-oligonucleotide structures – "Crab" aRNases – to investigate how supramolecular dynamic activity can be harnessed to drive higher turnover and faster kinetics, which would also scale into complex RNA biology, here demonstrated in knockdown of oncogenic miRNAs (oncomiRs). The thermodynamic stability of the heteroduplex is particularly rate-limiting, because bonds in the double-stranded region cannot be cleaved by catalytic peptides. However, the heteroduplex is also a dynamic supramolecular structure, where single strands arise sporadically as the edges of double-stranded regions fray.

The relatively high stability of *DNA-RNA* hybrids becomes an even greater challenge, particularly when longer recognition motifs are used, which inevitably reduce the off-rate constants to poorly-catalytic levels of slow exchange of longer (and still hybridized) RNA fragments with intact target RNA. Shortening the recognition domain here to 13 nt (Fig. 1, Table 1), reduced its binding affinity, so that the hybridizing complexes could more easily liberate fragments of cleaved RNA from the aRNase to enable a new catalytic cycle. Yet, the designed oligonucleotide recognition motif was long enough to form sufficiently stable *RNA-DNA* hybrids and provide sufficient sequence-specificity. We estimated the stability (T_m) and thermodynamic parameters (ΔG, ΔH and ΔS) of the predicted heteroduplexes between miR-17 or miR-21 and the recognition components of their corresponding "Crab" aRNases (Fig. S6) using the DINAMelt Server (www.unafold.org). According to these predictions, T_m values calculated for the hybridized complexes are sufficiently high (40.1 °C and 48.4 °C, respectively). We anticipated therefore that the close proximity of the predicted T_m values for these heterocomplexes to physiological temperatures (37 °C) will help tip the *association-dissociation* cycle, both *in vitro* and *in vivo*, in favor of catalytic turnover. We expect that competitive strand displacement, especially in excess of RNA substrate may reinforce this process further [54,55].

We compared mono-peptide analogues, by synthesizing two miR-21-targeted mono-peptidyl-oligonucleotide conjugates (5′-p-21 and 3′-p-21), bearing the same peptide attached either at the 3′-end (Fig. 1E and F) or 5′-end (Fig. 1G and H) of the recognition domain with the "Crab" conjugates (Fig. 1A–D), where two catalytic peptides were positioned to attack the functional region and increase the frequency of peptide attack on the hybridized RNA heteroduplex (best considered in 3D, Section 3.3).

The pair of 10-mer amphiphilic peptides Acetyl-$[LRLRG]_2$-COOH [36,37,39–41], each containing a regular arrangement of alternating basic (arginine) and hydrophobic (leucine) amino acids were attached to the recognition motive. It was postulated earlier [56–59] that the catalysis of cleavage of the RNA sugar-phosphate backbone is facilitated through simultaneous action of two arginine residues, when they are present in the same molecular structure. The synchronized action of two guanidinium groups of arginine amino acids, acting as a part of a *guanidine-guanidinium* dyad, enables the proton transfer between the attacking 2′-OH, non-bridging phosphate oxygen and departing 5′-O group within the RNA chain [40,41]. This facilitates the formation of a di-anionic pentaoxyphosphorane intermediate and ultimately promotes the transesterification reaction. The peptide arrangement used here

promoted catalysis, by providing increased opportunities to form *guanidine-guanidinium* dyads in close proximity to the RNA sugar-phosphate backbone, to catalyze the transesterification reaction [56,57,59,60]. In order to assess how this "Crab" arrangement of peptides at each end of the oligonucleotide recognition motif affected aRNase function, we generated three structural variants of peptidyl-oligonucleotide conjugation, with different orientations against the miRNA (see Fig. 1A–D).

The first structural variant (miR-21-targeted Crab-p-21) had the catalytic peptides flexibly attached to the 5′- and 3′-terminal phosphates *via* 5′-aminohexyl and 3′-6-amino-2-(hydroxymethyl)hexyl linkers, respectively (Fig. 1B). The other variants of "Crab" conjugates had the catalytic peptides conjugated to the 5′- and 3′-abasic deoxyriboses (dR) - flanking the recognition oligonucleotide - through aminohexyl linkers located at the anomeric C1′ carbon either in an α-configuration, structural variant 2 (Fig. 1C) or in a β-configuration, structural variant 3, (Fig. 1D). Structural variant 2 is represented here by Crab-α-21 and Crab-α-17, which were miR-21-specific and miR-17-specific aRNases, respectively, whereas structural variant 3 was exemplified by miR-21-targeted Crab-β-21 (Table 1).

Our challenge here was for each aRNase molecule to destroy *multiple* copies of oncogenic miRNA biologically, by simultaneous targeting two or more of its functional determinants upon sequence-specific hybridization, including the critically-important seed region (as the prime target site) and the 3′-terminal domain (as an additional target site). As the key initiator of post-transcriptional mRNA regulation, loss of this seed region should cause irreversible loss of miRNA functionality and trigger the desired biological effect. The destruction of the 3′-terminal regions would additionally destabilize functional complexes of *miRNA: AGO2*. The "Crab"-type aRNases developed here were targeted to highly oncogenic miR-17 and miR-21, recognized for their involvement in the etiology of multiple malignant diseases [61–64]. Cultured cell and tumor model studies included a non-specific Crab-α-Scr "control" conjugate (Table 1), which was synthesized with a scrambled non-targeted oligonucleotide component (Table S1).

3.2. Characterization of "Crab" aRNases and hybridization with RNA

The synthesis and full characterization of "Crab" aRNases are described in detail in the "Materials and Methods" section and in "Supplementary Information". The identities and purities of the conjugates isolated by RP-HPLC were confirmed using MALDI-ToF spectrometry and ^{1}H NMR spectroscopy (Fig. S1 and Figs. S2–S4). A shift in HPLC retention time from 18 to 19 min (for unconjugated oligonucleotides) to 24–25 min (for "mono" conjugates) and to 30–31 min (for "bis" conjugate) confirmed the attachment of one or two peptides, respectively. The MALDI-ToF mass spectrometric data reported in the "Materials and Methods" section and Fig. S1 showed that the experimentally-measured masses of the conjugates are in close agreement with the calculated values. The complete assignment of individual ^{1}H NMR signals to the specific peptide and oligonucleotide protons was difficult due to considerable spectral overlaps. However, careful comparisons between the NMR spectra of the conjugates (Figs. S2–S4) with those of the uncoupled oligonucleotides and peptides allowed us to verify successful peptide attachment. In particular, the characteristic peptide signals of Leu-H$^{\delta}$ and Arg-H$^{\delta}$ in the resonance areas of 0.8–1.2 ppm and 3.1–3.4 ppm, respectively, which resonate separately from oligonucleotide protons, provided evidence of the peptide presence in the sample. Also, careful signal integration in the NMR spectra confirmed the expected stoichiometric ratios of the attached peptide moieties to the oligonucleotide component (see "Materials and Methods").

Sequence-specific hybridization of aRNases with the target RNA is a vital step for selective RNA cleavage. We assessed the ability of the "Crab" recognition motif, here with reduced stability (T_m) and thermodynamic parameters (ΔG, ΔH and ΔS), to recognize and bind complementary miRNA targets by gel-shift assays. As the miRNA-specific "Crab" designs had similar oligonucleotide recognition scaffolds, we expected similar binding affinities to the respective miRNAs. Crab-α-21 and Crab-α-17 had close values of association constants, reaching $K_a = 0.35 \pm 0.05 \times 10^6\ M^{-1}$ for Crab-α-21 and $K_a = 0.34 \pm 0.09 \times 10^6\ M^{-1}$ for Crab-α-17. The gel-shift analysis also showed that Crab-α-21 and Crab-α-17 were able to efficiently bind [^{32}P]-labeled synthetic miRNA targets at a 5-fold excess over RNA, when the hybridization plateau was achieved, and the percentage of complexation reached 84 and 89 %, respectively (Fig. S7). Even with an increase in concentration (up to 10 μM), Crab-α-21 and Crab-α-17 conjugates were unable to quantitatively (100 %) bind their miRNA targets. A plausible reason could be that both miR-21 and miR-17 may form stable hairpins in dilute solutions with the estimated T_m values of 44.8 °C and 54.4 °C, respectively, and may also exist as partly complementary homomer duplex structures with predicted T_m values of 49.7 °C and 44.4 °C, respectively (Fig. S8A, C). In addition, the recognition motifs of Crab-α-21 and Crab-α-17 conjugates may also form intramolecular hairpin structures, but with lower estimated T_m values ranging between 35 °C and 37.1 °C, which are close to physiological temperature (Fig. S8B, D). The presence of folded and duplexed forms of miRNAs and oligonucleotides may potentially represent a thermodynamic hurdle for quantitative RNA binding.

3.3. Probability of miRNA bond attack in "Crab" heteroduplexes

Earlier Molecular Dynamics modeling of a small section of a related supramolecular assembly [36,40] identified the importance of the high flexibility of this conjugated peptide and the in-line attack by pairs of arginine residues for transesterification. The size and complexity of these supramolecular assemblies prevents consideration of the much larger scale of the dynamics of the whole heteroduplex assembly. Given this impasse, as a first effort to cast more light on the dynamics at this larger scale, heteroduplexes were constructed in 3D mathematical space (using Mathematica, Supplementary Method) to represent the supramolecular assemblies likely to dominate our empirical experimental studies. We could then tie this novel modeling at the larger scale to this empirical data. Unlike molecular modeling, this coarse model operated at a larger scale than atomic and molecular interactions, which allowed us to exclude any molecular forces and electronic properties and consider only the locations of every phosphodiester bond in 3 types of heteroduplex assemblies. The core heteroduplex assembled single RNA and peptidyl-oligonucleotide molecules (1:1 assembly). The 3D visualization presents bond regions (green spheres in Fig. 2A), with nucleotides and peptides superimposed (not intended to be a molecular model). Popular 2D cartoons may be compared (Fig. 2A left, cf Fig. 1A) but will misinform 3D interactions. This 1:1 core was essentially present in the other two possible molecular assemblies involving 3-strands, which were also considered here. Indeed, in the *initial* excesses of RNA over aRNase, two RNA molecules may also assemble with each peptidyl-oligonucleotide conjugate (to form 2:1 assembly, Fig. 2B). This 2:1 assembly may become one of the main supramolecular structures for attack by "Crab" peptide pincers, to provide a platform for competitive displacement and catalytic turnover. However, in these multiple turnover studies, the proportion of 2:1 and even 1:1 assemblies was expected to gradually decline as a result of rapid depletion of intact miRNA due to progressive cleavage. In the reciprocal excess, two peptidyl-oligonucleotide conjugates may potentially assemble with a single RNA molecule (to form a 1:2 assembly). However, as evident from our hybridization experiments (see Fig. S7), with the excess of aRNase (5 μM) over miRNA (1 μM), the core 1:1 assembly was predominant, but may become accompanied by minor levels of 1:2 assemblies, as miRNA cleavage progressed, thus leading to even further reduction of its concentration. Various hairpin and loop structures (Figs. S6 and S8) may be similarly introduced into this model, but were likely minor factors and were not introduced at this stage.

The location of each arginine (R) was also considered during the independent pseudo-random motions of each peptide. Close encounter

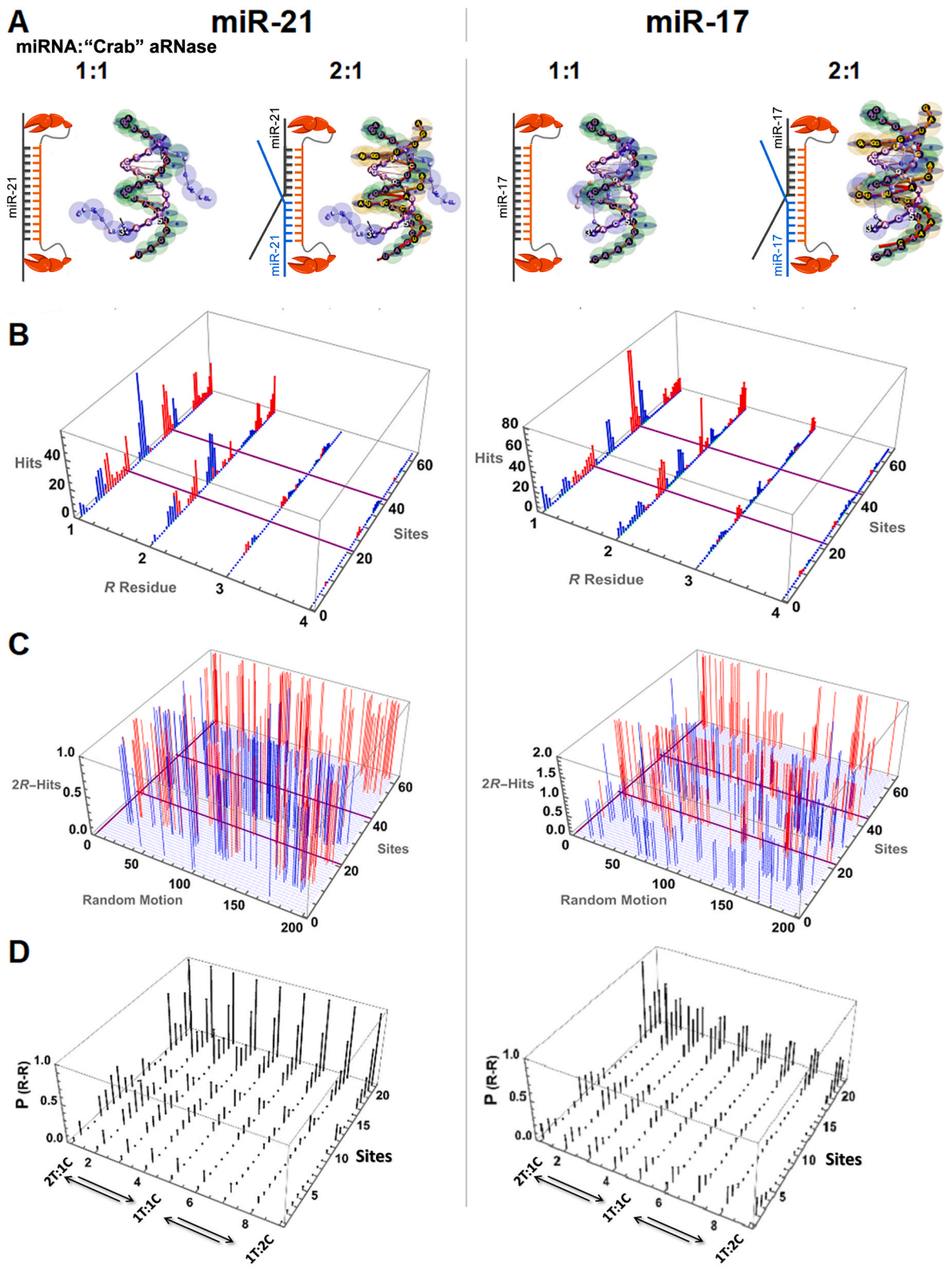

Fig. 2. Computed peptide collisions with miR-21 (left) and miR-17 (right). (**A**) 2D cartoon alongside 3D 1:1 core assembly (bond regions green spheres) and the 2:1 assembly with two miRNA strands and additional bond regions in the dangling lengths of each strand (yellow spheres), together with the regions of arginine residues (purple spheres). (**B**) Collisions of arginine regions, R: 1 to 4 from the site of peptide conjugation at 3'- (blue) and 5'- (red) ends, with bond regions were recorded over 200 pseudo-random motions, with (**C**) simultaneous collisions by two R residues (2R Hits) at each bond region for the 1:1 (5': 1–21 for miR-21, 1–22 for miR-17), dangling single strands in 2:1 (22–42 for miR-21 and 23–43 for miR-17) and from peptides on dangling conjugate strands 1:2 (43–63 for miR-21, 44–64 for miR-17) assemblies, for peptides conjugated at 3'- (blue) and 5'- (red) ends. (**D**) Probability P (R–R) of simultaneous collision against heteroduplex assemblies: 2:1 (1), 1:1 (5) and 1:2 (9), and for mixtures between (2:1 1:1 & 1:1 + 1:2) in the proportions 0.75 + 0.25 (2 & 6), 0.5 + 0.5 (3 & 7), 0.25 + 0.75 (4 & 8). (For interpretation of the references to colour in this figure legend, the reader is referred to the Web version of this article.)

of a R residue with a bond location (R 'Hit') and simultaneous close encounter of a bond location by a pair of R residues ('2R Hit') were recorded, including during fraying of the ends of each heteroduplex and zipping/unzipping motions of the 3 strand heteroduplexes. Most striking was the imprint of the 3D helical structure (Fig. 2A) on the profile of collisions with miR-21 and miR-17 (Fig. 2B). This profile appears substantially due to the helical structure, because each motion of each peptide, including the plane and angle in that plane, together with intrachain positioning and bending were all selected pseudo-randomly. The collision frequency declined along the peptide chain: highest for R_1 proximal to the conjugation site and smallest for the distal R_4, as may be expected geometrically for this tethered motion. The collision profile detail was sensitive (Fig. 2B and D) to the single base length difference of miR-17 longer than miR-21.

The 3′- and 5′-conjugated peptides predominantly attacked groups of bonds from different helical turns. Each peptide clearly demonstrated collisional selectivity for the helical loop more accessible by proximity to its R1 and R2 residues (Fig. 2B). The distal residues (R3 and R4) more readily collided with more distal bond regions, which overlapped with the greater collision frequency from the proximal residues (R1 and R2)

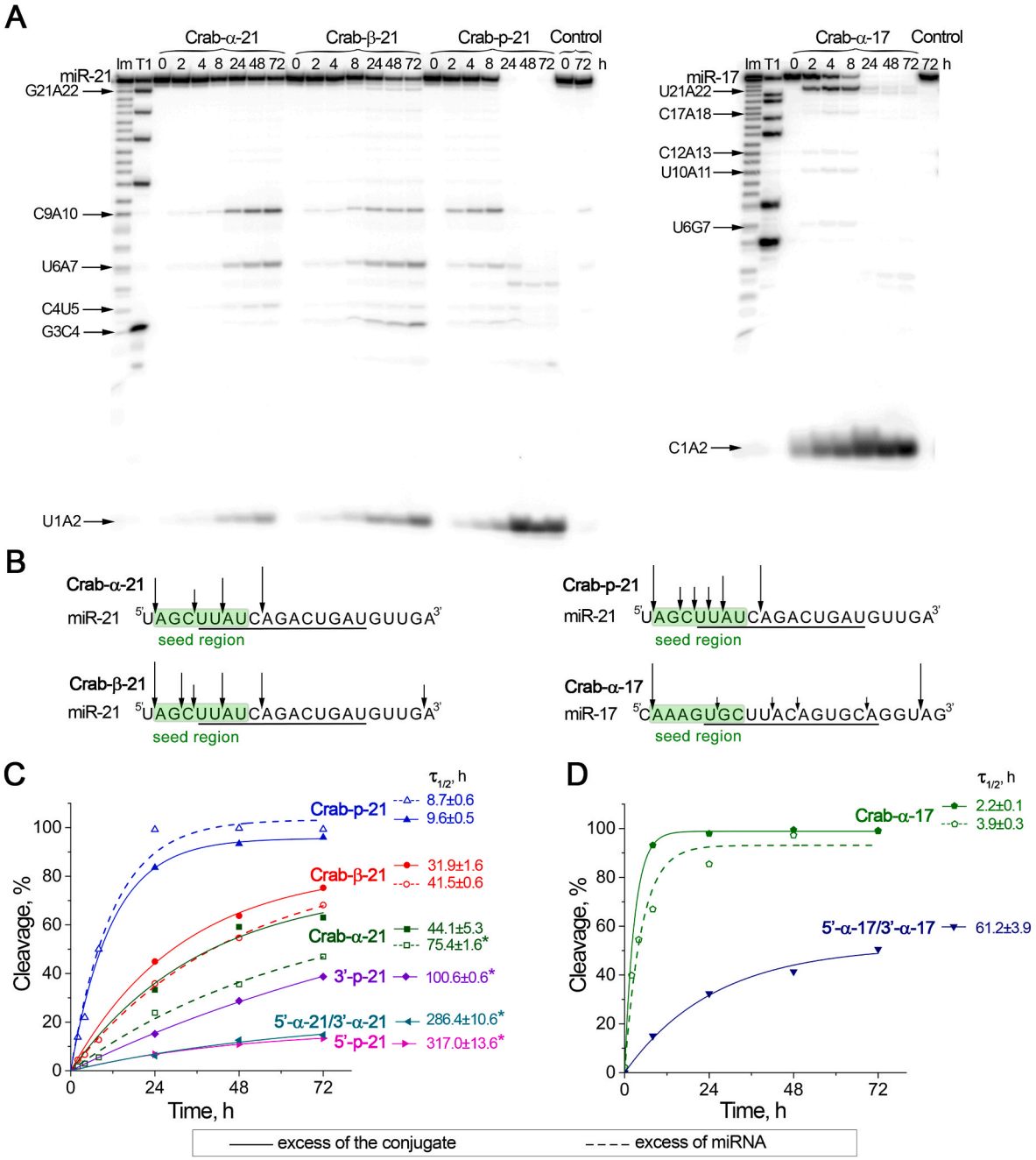

Fig. 3. Cleavage kinetics of 5'-[^{32}P]-miR-21 and 5'-[^{32}P]-miR-17 by "Crab" aRNases. (**A**) Radioautographs of 18 % denaturing PAAG showing the cleavage products of miR-21 and miR-17 after incubation with Crab-α-21, Crab-β-21, Crab-p-21 and Crab-α-17 conjugates. miRNA (10 μM) and the conjugate (5 μM) were incubated at 37 °C for 72 h in Buffer (1) with 1 mM EDTA to avoid cleavage by metal ions. Lanes Im and T1 – imidazole ladder and partial RNA digestion with RNase T1, respectively; Control – miRNA was incubated in the absence of conjugates. The incubation time (in hours) is shown at the top. (**B**) Positions of miR-21 and miR-17 cleavage by specific "Crab" conjugates, respectively. The underlined sequence denotes the miRNA region duplexed with respective aRNase. (**C, D**) Progress curves of miR-21 and miR-17 cleavage by miR-21-specific (**C**) and miR-17-specific (**D**) "Crab" conjugates: in the excess of the conjugate (1 μM miRNA, 5 μM conjugate) – solid line or in the excess of miRNA (10 μM miRNA, 5 μM conjugate) – dashed line. $\tau_{1/2}$ – half-life (h) of cleavage of miRNA by "Crab" aRNase (* – extrapolated values).

of the partner peptide.

Consequently, a broad range of collisions arose across the heteroduplex region of the 1:1 assembly (Fig. 2B): with as many (miR-17) or more (miR-21) simultaneous collisions by two R residues of the 3′-peptide with the 5′-heteroduplex as with the 5′-terminal region (Fig. 2C). Furthermore, in the case of the 2:1 assembly, with dangling single strands across the whole recognition motif, from each of the two RNA strands, the 3′-peptide showed higher collision frequencies in the complementary region towards the 5′ end. Similarly, the 5′-peptide reciprocally attacked the 3′ complementary and non-complementary region (Fig. 2C). When these respective collision frequencies were combined and scaled, the 3′-terminal regions clearly suffered greater probability of attack than the 5′-terminus, but more from attack of dangling single strands of the 1:2 assembly, with less difference between the single strand overhangs of the 1:1 assemblies (Fig. 2D). Importantly for catalytic turnover, attacks in the complementary region appeared likely, particularly corresponding to the dangling single strands of the 2:1 complex, likely present in excess miRNA conditions, and the fraying edges of the 1:1 heteroduplex also present here, and which also dominated under excess conjugate, single turnover conditions. Only minor levels of the 1:2 assembly may occur in cleavage studies, where attack probability shifted towards the terminal regions, with two peptides operating at each terminus. Similar findings arose for different size and shaped bond and R regions (see section *"13. Supplementary Results: 3D geometry selective for in-line R-R attack of bonds"* in the Supplementary Material).

3.4. Observed cleavage activity of "Crab" aRNases

We investigated the main factors affecting ribonuclease activity including: (i) arrangement of catalytic peptides in the "Crab"-type aRNases as compared to mono-peptidyl conjugates; (ii) attachment mode and configuration (α or β) of peptides; (iii) sequence of 5′- and 3′-single-stranded stretches of miRNA targets and (iv) sensitivity of bond cleavage to nucleotide base neighbors.

Two reaction conditions were considered here (Fig. 3 and Fig. S9). (1) *Single-turnover* reaction conditions (Fig. S9) had a 5-fold molar excess of aRNase (5 μM) over miRNA (1 μM), which represented the plateau level of binding (Fig. S7). These conditions were used mainly to investigate the activity of 1:1 assemblies of miRNA with the "Crab" aRNase for all of its structural variants. (2) *Multiple turnover* reaction conditions (Fig. 3) had a 2-fold molar excess of miRNA (10 μM) over "Crab" aRNase (5 μM), which allowed formation of 1:1 but likely also 2:1 molecular assemblies (Fig. 2A) with dangling single strands covering the entire complementary region.

Comparison of aRNases in *single-turnover* reactions analyzed their degradation of miRNA after one-only cleavage cycle, at least initially. The "Crab"-type arrangement of two peptides indeed had much higher cleavage activity compared to their counterparts possessing only one peptide either at 3′- or 5′-end (Fig. S9A and B, Fig. 3C). After 24 h, the extent of cleavage (%) of miR-21 by Crab-p-21 (84 %), Crab-β-21 (64 %) and Crab-α-21 (32 %) was considerably higher than that catalyzed by the mono-peptide conjugates 3′-p-21 (15 %) and 5′-p-21 (7 %). Even with a single turnover, the catalytic velocity enhancement was 5.6-fold and 12-fold for the corresponding Crab-p-21 bis-conjugate. (Fig. S9A, Fig. 3C, and for observed rate constants see Table 1). Ribonuclease activity was also evaluated for a 5′-α-21/3′-α-21 sample (Fig. S5), which represented by-products of the synthesis of Crab-α-21 (isolated by HPLC with retention time of 24–25 min), which contained a mixture of mono-peptide conjugates with either 3′- or 5′-mono-modification (confirmed by ^{1}H NMR, Fig. S4C). These non-separated by-products also showed low activity, achieving little (only 6 %) cleavage (Fig. S9A, Fig. 3C and Table 1), which was 5.3-fold lower than the related Crab-α-21. The considerably lower activity of the 3′- and 5′-monopeptides, both separately or in a mixture, strongly suggests much more than additive advantage of both the 3′- and 5'-"Crab" peptides. Explanation from the modeling studies illustrated the "pincer"-like attack of the "Crab" design, where both complementary and terminal regions were consistently more broadly and extensively attacked than by any single peptide alone (Fig. 2). The motion of either peptide alone was much less likely to collide with the corresponding distal non-complementary single strand and particularly the fraying edges of the heteroduplex, which would only be periodically-available as single strands. With the "Crab" configuration of peptides, both the terminal and heteroduplex regions proximal to each peptide were much more frequently attacked, where the 3′-terminus was attacked more than the 5′-region (Fig. 2). Similar levels of cleavage arose initially at both 3′- and 5′-ends (Fig. S9B, miR-17), and then, as the 5′-cleavage of label progressed, 3′-cleavage declined and became invisible (Fig. S9A, miR-21). Cleavage at 5′-labeled end left the (now unlabeled) fragment to be further cleaved.

Among the "Crab" aRNase designs, the fastest cleavage kinetics were observed for Crab-p-21, which exemplified the "Crab" configuration of highly-flexible peptides attached at the 5′- and 3′-terminal phosphates of the recognition oligonucleotide *via* 5′-aminohexyl and 3′-6-amino-2-(hydroxymethyl)hexyl linkers, respectively. Within 48 h, 94 % of the 5′-labeled miR-21 had already been cleaved. The half-life time of 9.6 ± 0.5 h estimated for Crab-p-21 conjugate was much (3–5 fold) shorter than that for both the Crab-β-21 (3.3-fold at $\tau_{1/2} = 31.9 \pm 1.6$) and the Crab-α-21 (4.6 fold at $\tau_{1/2} = 44.1 \pm 5.3$).

The higher ribonuclease activity of Crab-p-21 over both Crab-α-21 and Crab-β-21 was likely attributed to the greater flexibility of attachment of the catalytic peptides at the 5′- and 3′-phosphate groups of the oligonucleotide recognition motif *via* aminohexyl linkers, whereas abasic ribose units, either in α- or β-configuration are more conformationally-constrained. Presumably, the greater level of conformational freedom within the Crab-p-21 architecture enhanced the molecular mobility of the peptides to explore the heteroduplex, leading to increased probability of forming the guanidine-guanidinium dyads in the vicinity of accessible cleavage sites, in order to catalyze cleavage. The higher frequency of attack by the proximal peptide (Fig. 2B) translated into pairs of arginine resides approaching the sites of bonds both in the heteroduplex and dangling single strands, as well as the terminal regions (Fig. 2C).

The "pincer" attack from the "Crab" arrangement of peptides appeared key to success, as their combined action on the heteroduplex resulted in synergistic (rather than additive) enhancement of the velocity and extent of cleavage (cf. Crab-α-21 *vs.* 3′-p-21 and 3′-p-21). Indeed, loss of "pincer" attack, with either the 5′- or 3′-terminal peptide missing, considerably reduced the velocity of RNA degradation for the monopeptide conjugates, such that the half-life time for miR-21 cleavage increased by 10 fold ($\tau_{1/2} = 100.6 \pm 0.6$ vs. 9.6 ± 0.5 h) for 3′-p-21 and by 33 fold ($\tau_{1/2} = 317.0 \pm 13.6$ vs. 9.6 ± 0.5 h) for 5′-p-21 (Fig. 3C).

The superiority of the "Crab"-type arrangement was also seen over their mono-peptide analogues when the "Crab" recognition motif was replaced to be complementary to miR-17. Indeed, Crab-α-17 exhibited particularly high cleavage activity, reaching 98 % cleavage by 24 h, whereas the efficiency of miR-17 cleavage by a mixture of isolated but unseparated mono-peptide conjugates 5′-α-17/3′-α-17 (confirmed by ^{1}H NMR, Fig. S4D) was only 32 %. The half-life time of miR-17 cleavage increased 30-fold, from 2.2 ± 0.1 h for Crab-α-17 to 61.2 ± 3.9 h for the 5′-α-17/3′-α-17 monopeptide mixture (Fig. S9B, Fig. 3D and Table 1).

Analysis of RNA cleavage kinetics in the reaction with a 2-fold excess of miRNA substrate showed that the "Crab" aRNases were able to cleave multiple copies of miRNA with high efficiencies, similar to those in the *single-turnover* reaction mode (Fig. 3A, C and D). Indeed, within 24 h, the most active Crab-p-21 aRNase catalyzed degradation of almost all miR-21 with $\tau_{1/2} = 8.7 \pm 0.6$ (Fig. 3C and Table 1), while Crab-α-17 degraded about 85 % of miR-17 over the same period with a $\tau_{1/2} = 3.9 \pm 0.3$ (Fig. 3 D and Table 1), thus providing compelling evidence for their multiple turnover catalysis.

The "pincer" attack across the complementary region (Fig. 2) provided by the "Crab" arrangement of peptides appears instrumental in

providing the catalytic turnover, likely by enabling faster competitive displacement by intact miRNA of smaller fragments with lower binding stability, which would overcome the slow exchange between long fragments and intact RNA of similar binding stability. As the reaction progressed, weakly-bound small fragments would have provided toehold positions [54,55] for more frequent competitive displacement of fragments remaining bound through hybridizing intact RNA or longer RNA fragments. In this way, the "Crab" attack dynamics (Fig. 2) could provide the synergistic catalytic turnover observed.

3.5. Impact of supramolecular structure and base neighbors on bond cleavage

Profiles of miRNA cleavage by "Crab" aRNases had similar cleavage patterns under both *single-turnover* and *multiple turnover* reaction conditions (Fig. S9 and Fig. 3A, B), principally attacking the 5′- terminal regions, from the 5′-label experimental evidence alone. For both miR-21 and miR-17, the most sensitive bonds to "Crab" attack were pyrimidine-A sites within the miRNA sequence (Fig. S9 and Fig. 3A, B). With regard to miR-21, the primary cleavage sites at the 5′-terminal part of miR-21 were U1-A2, U6-A7, and C9-A10 bonds. The miR-21 cleavage profile also included cleavage at the C4-U5 bond. Crab-β-21, and to a lesser extent, Crab-p-21 also showed additional, although weak cleavage at the G3-C4 position of the 5′-terminus and G21-A22 at the 3′-terminus of the miRNA (Fig. S9C and Fig. 3B). It appears that the 5′-region of miR-21 is more susceptible to catalytic destruction than the 3′-end, despite indication of the greater peptide attack at the 3′-end (Fig. 2), likely in large part due to the presence of cleavage-sensitive bonds in this region of miR-21. As for miR-17, Crab-α-17 largely cleaved miRNA at pyrimidine-A sites within this sequence, with a predominance of cleavage apparent at the C1-A2 bond at the 5′ region and the U21-A22 bond at the 3′ single-stranded miRNA part. Additional weaker cleavage was also observed at the U10-A11 and C12-A13 positions, with very minor cuts at U6-G7 and C17-A18 sites, all were located within the central part of the heteroduplex (Fig. S9C and Fig. 3B). In general, it appears that the sensitivity of phosphodiester bonds to cleavage by "Crab" aRNases decreased in the order: pyrimidine-A ≫ pyrimidine-Y (where Y can be any of the three nucleotides C, G or U) > G-X (where X can be any of the four nucleotides A, C, G, U). This rank order is consistent with previous reports, which highlighted the 5′-U-A-3′ and 5′-C-A-3′ phosphodiester bonds as the most reactive and sensitive to RNA transesterification [59,65]. The effect of neighboring bases as well as distant nucleotide motifs has also been shown to contribute significantly to chemical stability of targeted phosphodiester bonds, presumably due to particular patterns in stacking interactions and hydrogen bonding [65–67]. Clearly, the nucleotide sequence of the miRNA, particularly within the double-stranded regions exposed for the synergistic catalytic attack of "Crab" peptides, plays a major role in determining the velocity and extent of catalysis by these "Crab" RNases, which can overpower even the effect from the thermodynamic stability of the hybridized complex. From our evaluations using DINAMelt Server of the heteroduplexes formed between miR-17 or miR-21 and the recognition oligonucleotide of their corresponding "Crab" aRNases (see Fig. S6), the T_m values calculated for the intact hybridized complexes appeared to be 48.4 °C and 40.1 °C, respectively. These figures suggested the higher stability of the miR-17-containing hybrid, which is consistent with the larger contribution from more stable G-C base-pairs to the duplex region (6 × G-C (46.2 %), 7 × A-T (53.8 %)) as compared to that of the miR-21-containing hybrid (4 × G-C (30.8 %), 9 × A-T (69.2 %)). One would expect therefore that the higher thermodynamic stability of the miR-17-containing hybrid should reduce the frequency of edge-fraying and/or strand-unzipping events, thus restricting the freedom of motion of the conjugated peptides, and decreasing the overall cleavage velocity. However, we observed the exactly opposite effect: the overall rate of miR-17 degradation by Crab-α-17 was nearly 20 times higher than that of miR-21 target by the structurally relevant conjugate Crab-α-21 both in *single-turnover* and *multiple-turnover* modes (see Table 1 and Fig. 3). Under the *single-turnover* cleavage conditions, the half-life time of miR-17 degradation was 2.2 ± 0.1 h, whereas that of miR-21 was 44.1 ± 5.3 h. Similarly, much quicker disappearance of miR-17 was seen for the *multiple-turnover* mode, with the half-life times being 3.9 ± 0.3 h and 75.4 ± 1.6 h for miR-17 and miR-21, respectively. This suggests that the hybridization power of the miRNA target appears to be less important for the rate of degradation than its oligonucleotide sequence, especially that part of the sequence which is involved in the formation of the heteroduplex with the "Crab" conjugates. Indeed, the presence of five (most vulnerable to cleavage) pyrimidine-A phosphodiester bonds (3 × C-A + 2 × U-A) in the sequence of miR-17 made this target more susceptible to cleavage by attacking peptides. In contrast, only three such linkages (2 × U-A + 1 × C-A) are present in the sequence of miR-21, thus making it slightly more resilient towards "Crab" aRNases.

One of the striking achievements of this work was the demolition of the seed region of the miRNA sequences, which was particularly evident for miR-21. Indeed, the most effective miR-21 specific conjugate Crab-p-21 cleaved miR-21 at G3-C4, C4-U5 and U6-A7 positions, thereby disrupting the connection between the key nucleotides within this functionally significant determinant, while less active Crab-β-21 and especially Crab-α-21 appeared to miss one or two hits in this region. Equally important though was the fact that these aRNases induced visible cleavage in the *heteroduplex* region of the hybridized miR-21 (Fig. 3 and Fig. S9), specifically at the U5-U6, U6-A7 and C9-A10 positions. The relative contribution from heteroduplex cleavage was more apparent under multiple turnover conditions (Fig. 3A), when dangling single strands in the 2:1 assembly can potentially provide additional opportunities for cleavage, and where miRNA competition and displacement surely must actively take place for longer fragments to be released by incoming intact miRNA for turnover to occur.

In the case of miR-17, the sequence of the seed region, specifically the shortage of pyrimidine-X bonds, may partly explain the lower level of degradation by "Crab" aRNases at this functional determinant. Cleavage of bonds other than pyrimidine-A (*e.g.,* U6-G7) also likely occurs, but possibly at a slower or masked rate. miR-17, which significantly surpasses miR-21 in terms of overall degradation rate (cf. k_{obs} for Crab-α-17 and Crab-p-21, Table 1), appeared to be particularly sensitive to the rapid removal of the 5'-[^{32}P]-label, when cleavage in the seed and/or complementary regions of miR-17 may well be underestimated. Any subsequent fragments generated after the cleavage of the first 5′-labeled nucleotide (5'-[^{32}P]-C1) become then invisible for detection, regardless of how quickly or efficiently they are produced. Yet, careful inspection of miR-17 degradation under *single turnover* conditions by Crab-α-17 (Fig. S9B) shows several cleavage products in the complementary region (at U6-G7, C17-A18 and particularly at the U10-C11 and C12-A3 positions), which become even more visible for the slower and less catalytically efficient 5′-α-17/3′-α-17 monopeptide conjugates, when less of the 5′-label had been cleaved and at much lower rate.

Unfortunately, there is no label-free laboratory method to follow cleavage fragmentation quantitatively to avoid the obvious limitation of reliance on label for this analytical detection (≪5 pmol). Even with advanced hyphenated mass spectrometry techniques, it is not possible to separate and quantify (by HPLC, CZE) fragments of the same length, but with different nucleotide composition, without using a label for fragment identification. However, given the importance of cleavage in the heteroduplex and base neighbors in bond cleavage, we analyzed cleavage patterns further by investigating the likelihood of in-line attack of bonds by pairs of arginine (R-R) residues [40], using the 3D computational models of the *miRNA:Crab RNase* heteroduplex assemblies (Fig. 4A, for details see Supplementary Method).

We first investigated the basis for selection of in-line R-R attacks of bonds within the mi*RNA* – "Crab" aRNase assemblies. We set 3D regions around each bond (spherical and elliptical in Fig. 4A), and allowed the pseudorandom motions of the peptides to explore the accessibility of these regions to pairs of R residues ('2R Hits' Fig. 2C). Despite the higher

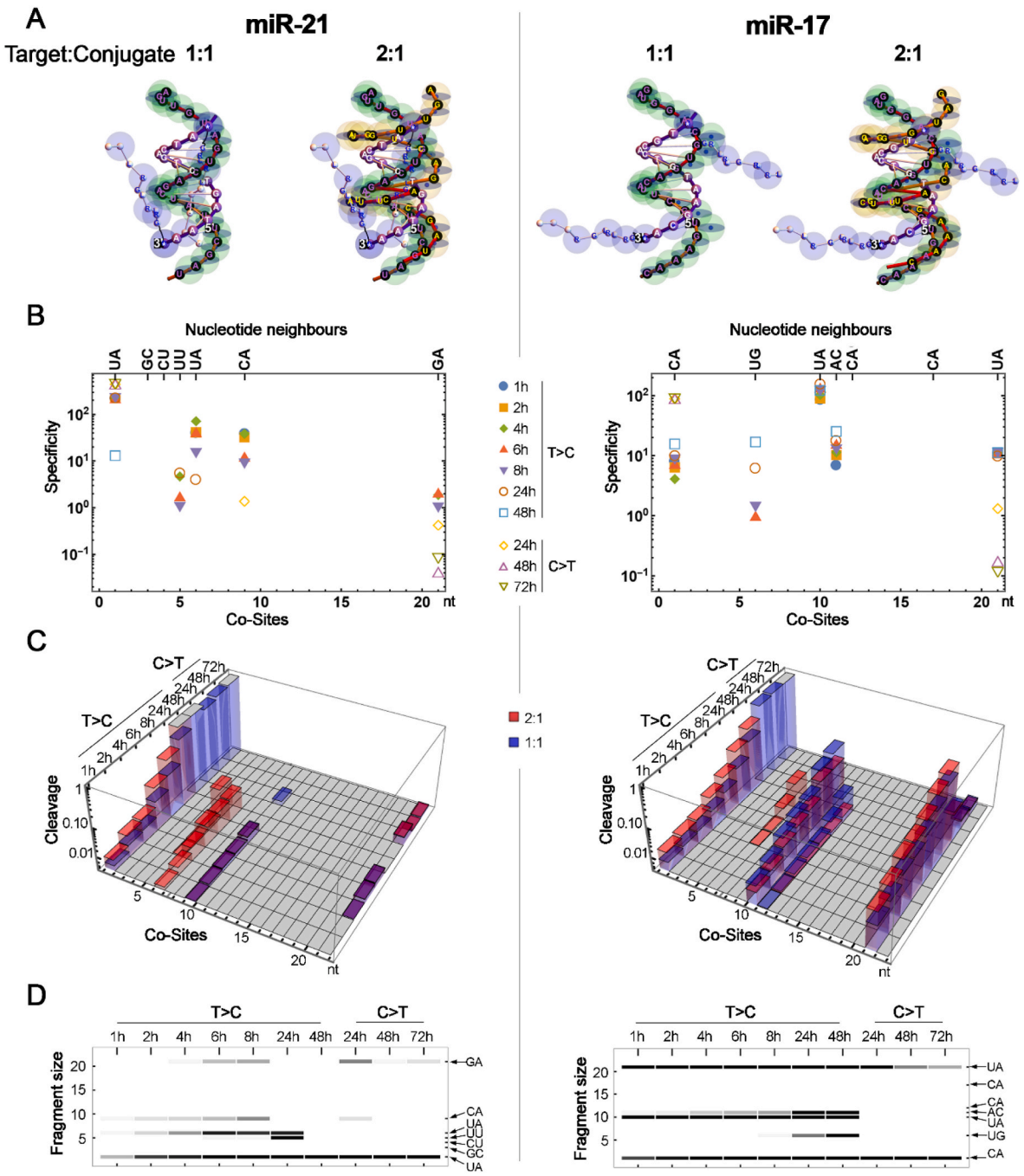

Fig. 4. Simulation of fragment cleavage by miR-21 (left) and miR-17 (right) "Crab" aRNases. (**A**) Images of 3D geometric models of 1:1 and 2:1 (Target: Conjugate) complexes with regions of pseudo-random interaction between R (purple spheres) in the peptide chains and cleaving sites in the 1:1 (green spheres) and dangling single strands of 2:1 complexes (yellow spheres), each with a horizontal elliptical region used for estimation of coincident R-R in-line attack (Co-sites). (**B**) The specificity of cleavage at each site. (**C**) Relative contributions of 1:1 (blue) and 2:1 (red) complexes to the simulation (**D**) of 5′-fragment patterns observed (in Fig. 3). (For interpretation of the references to colour in this figure legend, the reader is referred to the Web version of this article.)

frequency of these R-R attacks at the 3′-region (see section *"Supplementary Results: 3D geometry selective for in-line R-R attack of bonds"* in the Supplementary Material), greater cleavage was visible *experimentally* at the 5′-region, predominantly because of the higher cleavage specificity of bonds with the nucleotide neighbors at the 5′-region and because cleavage of remaining large (but now unlabeled) fragments became invisible. When the probability of in-line R-R attacks (see Supplementary Results, page 28) was used to minimize the contribution from helical superstructure effects, associated with R-R bond attacks, from the cleavage of bonds observed experimentally, the resulting estimates of the cleavage specificities of bonds with different base neighbors ranged over two orders of magnitude (cf U-A and G-A cleavage specificity for miR-21, or C-A and U-G cleavage specificity for miR-17 in Fig. 4B), reminiscent of the range of chemical stabilities of oligonucleotide bonds [65].

During the early stages of the multiple turnover reactions, under excess target conditions (filled symbols in Fig. 4B, from 1 to 8 h), the high U-A cleavage specificities were of similar order, whether for the greater extent of cleavage of the 5′-region of miR-21, or for the lesser extents of cleavage observed for the duplexing regions of miR-17 and miR-21. Likewise, the mid-range C-A cleavage specificities were also of similar order, whether located at the 5′-region of miR-17, or for the

lesser extent of cleavage when located at the duplexing region of miR-21. Single turnover reaction conditions with excess conjugate elevated the cleavage specificity of the key 5′-region sites (C-A in miR-17 and U-A in miR-21), but diminished the specificity of the U-A site at the 3′-region of miR-17. Analysis of attacks of spherical regions alone showed a similar ranking of specificities over a marginally narrower range for the same nucleotide base neighbors, but with bias towards the contribution of dangling strands, likely due to inclusion of 'near misses' (Fig. S10 and Fig. S11). Similar nucleotide base-neighbor specificities were estimated for elliptical regions and their coincidence with an embedded small spherical region, which likely excluded 'near misses' from the axial direction (Fig. S12 and Fig. S13), but included the fewer arising around the periphery of the equatorial region, which were minimized by the main geometry selected to discern probable in-line R-R attack (Fig. 4A).

Our premise for the work here appeared to be a reasonable first approximation, that the cleavage patterns observed experimentally were substantially the product of the probability of R-R attack of each bond (heteroduplex superstructural effects) and the probability of its cleavage when attacked ('specificity'). This allowed this cleavage specificity to be extracted from experimental data by minimizing the structural effects associated with R-R attack of bonds constrained by heteroduplex superstructure. The width of 'specificity' for bonds with the same nucleotide base-neighbors (located in different positions in the miRNA, or different miRNA) likely reflected the additional finer structural factors around different bonds with the same nucleotide-neighbors [65]. With the effects of heteroduplex superstructural constraints minimized, the nucleotide base-neighbor specificity of this R-R catalysis may relate substantially to the base preferences of the transesterification reaction of this catalyst, with similar meaning to the 'base specificity' of nuclease enzymes.

The relative contributions of the different secondary structures of the assemblies considered (2:1, 1:1 and 1:2) were available within the frequencies of R-R attacks of each bond at its different structural locations. This allowed the contribution of the additional strands and site dispositions in complexes to be considered. Dangling miRNA single strands in 2:1 assemblies contributed strongly to the simulated cleavage patterns (red in Fig. 4C), substantially from the non-complementary single-stranded regions, alongside cleavage of these regions overhanging the 1:1 heteroduplex within the assemblies (blue in Fig. 4C). The cleavage of bonds in the region complementary to the antisense oligonucleotide of the aRNase was also analyzed. This arose from the dangling single strands in 2:1 complexes (red in Fig. 4C), and from the edge fraying of the double-stranded regions within the 1:1 heteroduplex (blue in Fig. 4C). Given the more rapid cleavage of the 5′ non-complementary region, bearing the [^{32}P] label used, electrophoretic cleavage patterns may underestimate the velocity and extent of cleavage in the complementary region. This may explain the lower estimates of specificity of bonds in the complementary region compared with bonds in the non-complementary region with the same nucleotide base neighbors (Fig. 4B). Cleavage in these complementary regions is particularly important to increase turnover by promoting displacement of shorter RNA strands cleaved in the double-stranded region with intact strands of RNA, including the cases with the synergistic action of RNase H cleavage at different sites. Dangling aRNase antisense strands and their conjugated peptides contributed less to cleavage at the 5′-end, and only to a small relative extent at the 3′-region (Fig. 3C). Dynamic unzipping and zipping motion periodically brought peptides and dangling strands into R-R attack range for a broader range of bonds, but also distanced the 3′- and 5′-regions from frequent attack (Fig. S14 and Fig. S15 for miR-21, and Fig. S16 and Fig. S17 for miR-17).

The 5′-fragment patterns observed experimentally in electrophoretic gels (Fig. 3 for excess target and Fig. S9 for excess conjugate) could be approximated by simulations (Fig. 4 D) combining the specificity (Fig. 4 B) and the relative frequencies of in-line R-R attacks (Fig. S18 and Fig. S19 for miR-21, and Fig. S20 and Fig. S21 for miR-17) at each cleavage site. Finally, the coincidence of spherical-elliptical R-R attack used here was confirmed by the much lengthier calculations of coincident attack of different octants of the spherical region for the R-R attack miR-21 (Fig. S22) and miR-17 (Fig. S23).

3.6. Synergistic action of "Crab" aRNases and RNase H in vitro

The efficiency of canonical antisense technology is based on the recruitment of intracellular nucleases, in particular, RNase H. A continuous stretch (13-nt) of the unmodified DNA scaffold within the "Crab" aRNases provides the opportunity to form a sufficiently-extended heteroduplex that can be recognized and attacked by the endonuclease, RNase H. Previously, we have shown that the presence of peptides in the structure of aRNases did not prevent the recognition and enzymatic cleavage of miRNAs duplexed with aRNase by RNase H. Moreover, aRNase and RNase H, when applied simultaneously, strongly enhanced the rate of miRNA cleavage through synergistic action [37–39,43]. We compared the cleavage of miRNA by: (1) aRNase alone; (2) by combined action of "Crab" aRNase (Crab-p-21 or Crab-α-17) and RNase H and (3) by RNase H alone when miRNA was pre-hybridized with peptide-free oligonucleotide (ON-21 or ON-17) (Table S1).

Importantly, in the presence of magnesium ions (8 mM $MgCl_2$), recommended for *in vitro* action of RNase H, "Crab" aRNases exhibited delayed cleavage kinetics (Fig. S24 and Fig. S25). Crab-p-21 had a 12 h lag phase followed by a sharp exponential rise, attaining 98 % cleavage efficiency by 24 h, and overtaking the level of cleavage observed in magnesium-free buffer conditions (Fig. S24 A and Fig. S25 A). Crab-α-17 demonstrated considerable retardation of miRNA cleavage kinetics, when overall cleavage was reduced by half (49 %, Fig. S24 B and Fig. S25C). According to DINAMelt calculations, the melting temperature of miR-21/Crab-p-21 and miR-17/Crab-α-17 duplexes in the presence of magnesium ions increases by approximately 2 °C (from 40.1 °C to 42.7 °C and from 48.4 °C to 50.6 °C, respectively) compared to magnesium-free buffer. The duplex stabilization effect of magnesium ions [68] manifests itself also in the strengthening of intramolecular structures present in both miRNAs and aRNases (Fig. S8), potentially leading to a reduction or retardation in formation of *miRNA:aRNase* complexes as dynamically available for cleavage of miRNA. Additionally, the stabilizing effect of magnesium ions may also diminish dissociation rates of cleaved fragments from heteroduplexes, thus limiting the number of reaction turnovers.

For cleavage studies with RNase H, we deliberately chose a relatively low concentration of RNase H (5 U/mL), to allow a comparative analysis of the efficiency of miRNA cleavage under conditions of sharp exponential growth of the accumulating products, resulting from joint catalysis by aRNase and RNase H. Under these conditions, RNase H acting alone, while guided by miRNA-targeted oligonucleotides (ON-21 or ON-17) showed very low cleavage of miR-21 and miR-17, reaching only 9 % after 48 h (Fig. S25B, D and Fig. 5G, H). Clearly, RNase H failed to act with catalytic turnover, presumably attached to the heterocomplex but catalytically unavailable.

The situation changed dramatically when RNase H and aRNase were used together, in the same incubates against respective targets (either miR-21 or miR-17), which sharply enhanced both the rate and extent of miRNA cleavage (Fig. 5 and Fig. S25). In the presence of both enzymes, the gain in the cleavage rate was most clearly detected in the first few hours (Fig. 5A, B, E, F). Already within 4 h of incubation, the efficiency of miR-21 cleavage reached 70 %, when Crab-p-21 and RNase H were used together, whereas their separate actions led to only 4 % of miR-21 degradation over the same period (Fig. 5E). Similarly, degradation of miR-17 by Crab-α-17 and RNase H, in a combined action reached 38 % within the first 4 h, but when acting independently, they cleaved miR-17 much less, by only 12 % for Crab-α-17 and 4 % for RNase H (Fig. 5F). Interestingly, miR-21 was more susceptible to synergistic catalytic cleavage by "Crab" aRNase and RNase H than was miR-17. Quantitative (100 %) cleavage by a combination of Crab-p-21 and RNase H was achieved for miR-21 within ≈12 h, whereas miR-17 was only fully

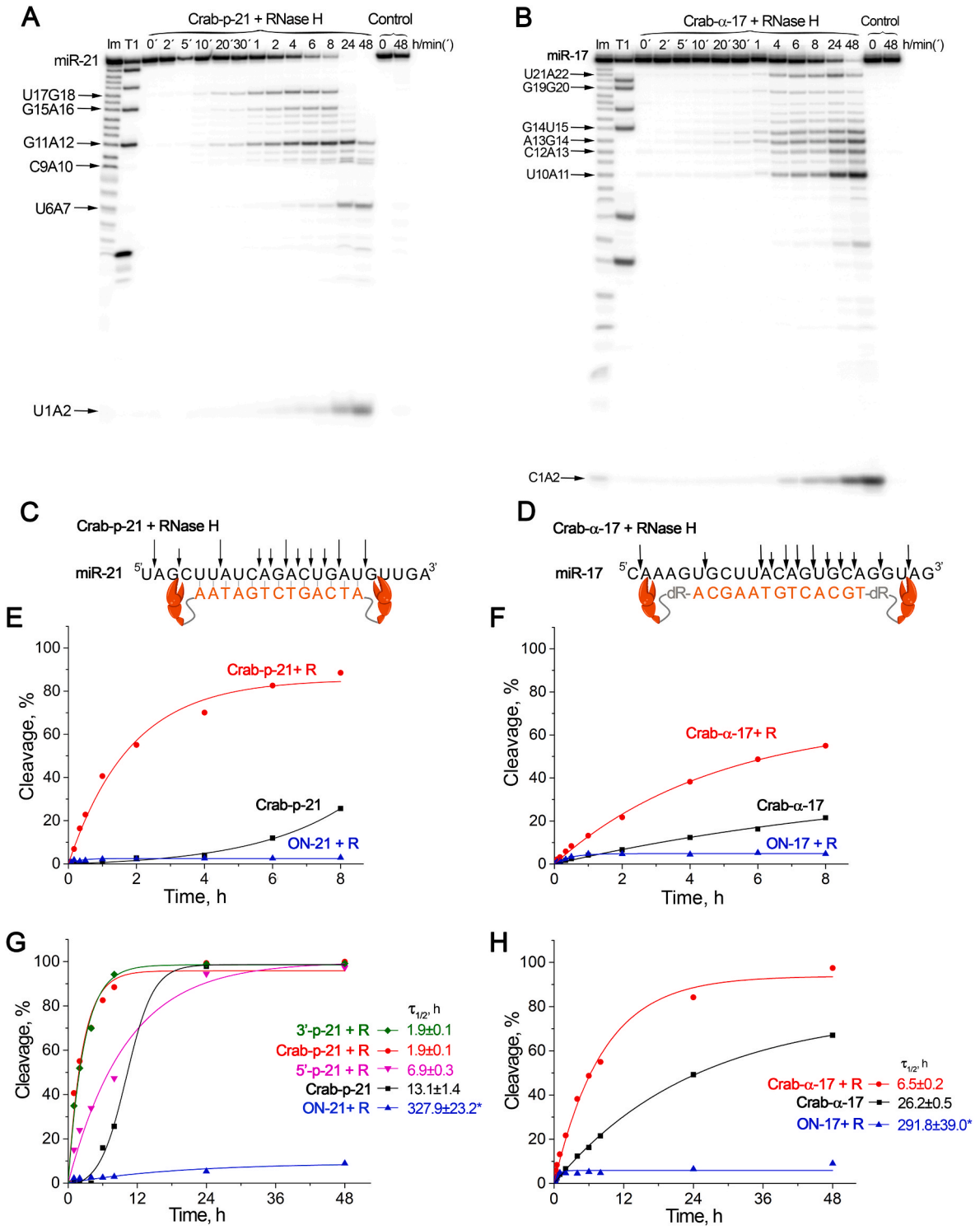

Fig. 5. Synergistic cleavage of 5'-[^{32}P]-miR-21 and 5'-[^{32}P]-miR-17 by "Crab" aRNases with RNase H. (**A, B**) Radioautographs of 18 % denaturing PAAG show the profiles of miR-21 and miR-17 cleavage by combination of Crab-p-21 and RNase H (**A**) and by Crab-α-17 and RNase H (**B**). Duplexes formed by 5'-[^{32}P]-miRNA (10 μM) and aRNase (5 μM) were incubated in Buffer (2) at 37 °C for 48 h. RNase H was used at 5 U/mL throughout. Key: lanes Im (imidazole ladder) and T1 (partial RNA digestion with RNase T1); incubation time shown at the top either in minutes (') or hours. Control – RNA incubated in the presence of RNase H but absence of aRNase and oligonucleotide. (**C, D**) Positions of miRNA cleavage by Crab-p-21 (**C**) and Crab-α-17 (**D**) conjugate and RNase H. (**E, F**) Progress curves of miR-21 and miR-17 cleavage by Crab-p-21 (**E**) and Crab-α-17 (**F**) and/or RNase H during the first 8 h of incubation. (**G, H**) Progress curves of miR-21 and miR-17 cleavage by Crab-p-21, 5'-p-21, 3′-p-21 (**G**) and Crab-α-17 (**H**) and/or RNase H during 48 h of incubation. R – RNase H. $\tau_{1/2}$ – half-life cleavage of miRNA in the presence of catalyst (in hours, * – extrapolated values).

cleaved after 48 h (Fig. 5G, H). The half-life time of miR-21 cleavage catalyzed jointly by the two enzymes was 1.9 ± 0.1 h, which was 7-fold shorter than that measured for Crab-p-21 and 172-fold shorter than RNase H, when working independently from each other (Fig. 5G). In contrast, the half-life of miR-17 cleavage for co-joint catalysis with Crab-α-17 and RNase H was 6.5 ± 0.2 h, which was shorter by only 4-fold for Crab-α-17 alone and 45-fold for RNase H alone (Fig. 5H). The differences observed may be attributed to various factors: (1) the nucleotide sequence and (2) thermodynamic parameters of intramolecular structures of different miRNAs in the presence of magnesium ions and (3) "Crab" architecture. Specifically, the presence of dR in Crab-α-17 may in some extent restrict the mobility of peptides thus limiting its synergistic action with RNase H.

The combined ribonuclease activity of "Crab" aRNase with RNase H accelerated by orders of magnitude, underlining the synergistic nature of their functioning together against miRNA (Fig. 5 and Fig. S25), with a dramatic increase in the accumulation of cleavage products catalyzed by RNase H in the central region of the heteroduplex (Fig. 5A–D). Electrophoretic images show that the RNase H endonuclease attack affected all bonds in the RNA molecule starting from the 5th nucleotide of the formed *RNA-DNA* heteroduplex, presumably because the first 5 nucleotides serve as the recognition and loading site for RNase H. It was also evident that the presence of RNase H induced additional capabilities of "Crab" aRNases, manifested by the appearance of new reaction products. The miRNA cleavage profiles were additionally supplemented by extra cleavage at the U17-G18 bond for Crab-p-21 and G19-G20 for Crab-α-17 (Fig. 5A–D), which were extensively attacked by the 3′-peptide (Fig. 2).

It was important for us to understand though whether both catalytic "pincers" are essential for this synergy with RNase H, and if so, which site of their attachment (3′- or 5′-end) is more critical for catalysis. To answer this question, we investigated the cleavage of miR-21 catalyzed by the joint action of RNase H with either 5′-p-21 or 3′-p-21 "single-pincer" conjugate (see Fig. 5G, Fig. S26A). Although the individual catalytic activities of 5′-p-21 or 3′-p-21 alone (*i.e.,* in the absence of RNase H) were virtually undetectable under these conditions (Buffer (2)) (Fig. S26B), the recruitment of RNase H led to significant enhancement in the rate of miR-21 degradation, which was 3.6-times more pronounced for 3′-p-21 than that seen for 5′-p-21. Indeed, the enhancement factor of enzymatic activity of RNase H in the presence of 3′-p-21 was 172-fold (similar to that seen for Crab-p-21), while in the presence of 5′-p-21 the activity of RNase H was enhanced by only 47.5-fold. This finding confirmed the dominant role of the peptide located at the 3′-terminus for the synergy with RNase H, which was also noticed for their individual actions (see Fig. 3). The attachment of the catalytic peptide at the 3′-position relative to the recognition oligonucleotide, and thus aligning it against the 5′-terminus of the target miRNA, appears to be crucial for enabling the synergistic action of this type of aRNases.

Undoubtedly, a powerful synergy is at work harnessing the differences in mechanistic action between these natural and synthetic enzymes. As RNase H cannot operate on the dangling single strands of 2:1 assemblies, this synergy arises from their joint action on the 1:1 heteroduplex region. The "Crab" aRNase can only act on the fraying edges of the heteroduplex, whereas RNase H acted in the middle of the heteroduplex in the less-dynamic double-stranded region, but where the initially-rapid action of RNase H appeared to stall, and fail to turnover when acting alone at low ratios, presumably because it remained attached to the cleaved heteroduplex. Accordingly, the enormous boost in the rate and extent of miRNA cleavage may be explained by the simultaneous action of "Crab" aRNases and RNase H at their different mechanistic locations, resulting in greater turnover of both: (1) rapid turnover of the "Crab" aRNase triggered by RNase H through the additional cleavage of fragments in the central double-stranded region of the heteroduplex, which inevitably reduced the size of the cleaved products and promoted their release; and (2) dramatic increase in the turnover of RNase H by aRNase cleavage of edge regions, including the loading site for RNase H at the 5′-end of the RNA part of the heteroduplex, presumably promoting rapid liberation of RNase H to initiate the next cycle of its enzymatic action. Together, this would have readily allowed free, intact miRNA to hybridize with the aRNase, when locally-released RNase H could rejoin synergistic action. The combination of the synergistic mechanism of "Crab" aRNase with the synergy of action with RNase H would become even greater biologically by "Crab" aRNase attack of the seed region of miRNA, unavailable to RNase H.

3.7. Biological activity of "Crab" aRNases

Biological application focused on the challenge of miRNA down-regulation in cultured cells and *ex vivo* in mice by "Crab" aRNases. miRNA molecules, compared to other types of intracellular RNA, are characterized by high intracellular levels, as well as biological stability and longevity [35,45]. miR-21 is one of the most highly-represented miRNAs in various eukaryotic cells, whose expression is even further raised during neoplastic transformation. Depending upon circumstances, its intracellular concentration can vary typically from 0.5 to 22 μM [35,69]. Since the addressing domain of the "Crab" aRNase is represented by an unmodified DNA oligonucleotide, to provide a sufficient concentration in the presence of intracellular nucleases, we used a transfection concentration of 1 μM to study the biological effects of "Crab" aRNases in cultured cells. Given the high level of target miRNAs, this concentration cannot reach a stoichiometric balance between aRNases and the miRNAs inside the cell.

The ability of "Crab" aRNases to reduce the level of specific miRNAs in cells was studied in human breast adenocarcinoma MCF-7 cells, which are characterized by high levels of miR-21 and miR-17. The effect of "Crab" aRNases specifically towards these miRNAs was measured against the control conjugate Crab-α-Scr (for sequence see Table 1). Similar to miRNA-specific aRNases, Crab-α-Scr comprised two catalytic peptides and an oligonucleotide devoid of any homology within the mammalian genome. The ability of Crab-α-Scr to induce cleavage in RNA was tested in a separate experiment (Fig. S27) through its incubation with synthetic 5'-[^{32}P]-miR-21 and 5'-[^{32}P]-miR-17 using the same reaction conditions as those for the miRNA-specific aRNases, with 5-fold excess of Crab-α-Scr conjugate (5 μM) over miRNA (1 μM). Crab-a-Scr exhibited some minor cleavage activity towards miRNAs in Buffer (1), with only 14 % cleavage observed for miR-21 and 9.4 % for miR-17 over a 24-h period (Fig. S27, Table 1). Functionally-active RNAs within the cellular environment are typically sequestered within nucleoprotein complexes, shielded by constituent proteins. Consequently, the substantial silencing effect is expected to be achieved with the direct integration of ribonuclease into the nucleoprotein complex, ensured by the sequence-specific affinity of the inhibitor towards the target RNA, the heteroduplex formation and synergistic action with RNases H. Considering the limited ribonuclease activity of control Crab-α-Scr conjugate and its inability to bind any RNA within the cell, we anticipate no nonspecific effects resulting from its application.

The additional advantage of the "Crab" configuration of our aRNases was the protective positioning of two catalytic peptides at the flanking locations of the recognition motif, which provided shielding of the "naked" deoxyribonucleotide recognition motif from cleavage by exonucleases at its 5′- and 3′-termini. Using Crab-α-Scr as a representative model, we evaluated the biological stability of "Crab" aRNases by exposing it to culture medium containing 10 % FBS, a standard concentration for cell cultivation and experiments. Published data suggest that 10 % FBS exhibits nuclease activity equivalent to or even exceeding that of adult human serum [70]. The gel electrophoretic analysis of the treated Crab-α-Scr and the corresponding unmodified oligonucleotide revealed (Fig. S28) that the nuclease resistance of "Crab" conjugate significantly surpassed that of the peptides-lacking oligonucleotide. The rapid disappearance of "naked" ON-α-Scr followed usual exponential kinetics, with estimated initial velocity of 125 %/h. However, the degradation kinetics for Crab-α-Scr could be deconvoluted into two

main parts: (i) an initial exponential component, with velocity of 34.5 %/h, and (ii) subsequent linear component with velocity of 0.33 %/h. Notably, the initial exponential loss of intact conjugate Crab-α-Scr, which was already 3.6-fold slower than that for ON-α-Scr, was followed by long-lasting linear degradation of the remaining 40–50 % of conjugate, which was 378 times slower than that for the "naked" oligonucleotide (Fig. S28B). Even after 72 h of incubation, a notable portion (≈15 %) of the intact conjugate remained detectable, while the unmodified oligonucleotide completely degraded within the first 2 h of incubation. Such level of nuclease resistance is not very different from that seen for the chemically-protected anti-miRNA oligonucleotide analogues broadly used in translational research [71]. The "Crab" aRNases appear to exhibit greater stability as compared, for example, to DNA/LNA and 2′OMe/LNA mixmers, which degrade completely within 6 h under 10 % serum conditions, and they demonstrate similar nuclease stability to DNA, LNA, and DNA/LNA mixmers, which are additionally protected by incorporation of the three phosphorothioate linkages at their 5′- and 3′-termini [71].

To deliver aRNases into tumor cells, we employed the widely-used, commercial transfection agent Lipofectamine™ 2000. The efficiency of Lipofectamine™ 2000-mediated accumulation of aRNases in MCF-7 cells was examined using Cy5.5-labeled 5′-α-21/3′-α-21. Flow cytometry analysis revealed that 4 h after transfection 99 % of cell populations became Cy5.5-positive with the average cell fluorescence (RFU), equal to 213×10^3, against 0.9×10^3 for Lipofectamine™ 2000 only (Fig. S29). In the absence of the transfection agent, Cy5.5-labeled conjugate was able to penetrate 99 % of MCF-7 cells, but with fluorescence almost an order of magnitude lower than that seen for the Lipofectamine™ 2000-mediated accumulation, achieving RFU of only 40×10^3. One possible reason for the limited ability of the "naked" conjugates alone (without the aid of any transfecting agents) to penetrate cells could be the remaining net negative charge (−6) on the "Crab" conjugates, as they contain 14 negatively-charged phosphate groups and only 8 positively-charged arginine residues. This suggests that longer peptide chains with multiple arginine residues might be necessary for more efficient uptake of "naked" conjugates."

The investigation of the impact of Crab-a-Scr on the level of target miRNAs in MCF-7 cells revealed that Crab-a-Scr does not exert any inhibitory effect on miR-21 and miR-17. The inhibitory action of specific "Crab" aRNases was weighed against the effect of corresponding miRNA-targeted oligonucleotides lacking any catalytic peptides. Analysis of miRNA inhibition kinetics showed that the most significant target downregulation both by "Crab" aRNases and oligonucleotides was observed within 24 h (Fig. 6A and B). Among the miR-21 targeted aRNases, Crab-p-21 had the greatest inhibitory effect, reducing miR-21 levels by approximately 65 % (Fig. 6A). By 48 h, miR-21 expression was restored to 50 % and remained at this level up to 72 h. Crab-β-21 demonstrated the lowest effect of about 30 % reduction of miR-21 levels by 24 h, which was a similar effect to the ON-21 antisense element alone (Fig. 6A). The superior silencing effect of Crab-α-17 (58 %) over ON-17 antisense oligonucleotide (40 %) was evident after 24 h (Fig. 6B). Generally, for both targets, the inhibitory trends of aRNases were more substantial and persisted for longer than with antisense oligonucleotides alone.

The selectivity of the aRNase-mediated silencing effect was assessed by analyzing the level of miRNA let-7g. Neither miR-21 nor miR-17 specific aRNases affected the expression of let-7g at 24 h (Fig. S30), while effectively reducing the levels of their respective complementary targets (Fig. 6 A and B).

Furthermore, the specificity of the inhibitory effect exerted by "Crab" aRNases was evaluated through the analysis of alterations of the levels of proteins regulated by miR-21 and miR-17. The downregulation of miR-21 by Crab-α-21 and Crab-p-21 led to the derepression of a tumor suppressor, PDCD4 (programmed cell death 4) [72], increasing the protein level in MCF-7 cells by 1.35 and 1.7-fold, respectively (Fig. 6C). Similarly, the suppression of miR-17 results in a significant elevation in the levels of E2F1 protein [63] by 1.9-fold and the cellular adhesion protein E-cadherin [73] by 1.5-fold in MCF-7 cells (Fig. 6D and E). These findings confirm the sequence-specific nature of action of the engineered miRNA inhibitors.

Upregulation of miR-21 and miR-17 is directly associated with the key hallmarks of tumor growth, such as uncontrolled proliferation and evasion from apoptosis, increased migration and invasion [74–76]. Targeted silencing of miR-21 and miR-17 should inalienably lead to suppression of tumor cell proliferation. We analyzed the viability of three tumor cell lines, including human breast MCF-7 and lung A-549 carcinoma and murine melanoma B16, after transfection with the respective aRNases, by using WST analysis to assess the ability of miR-21 specific "Crab" aRNases to inhibit the proliferative activity of tumor cells.

WST assays revealed the antiproliferative effect of aRNases. Crab-α-21 and Crab-β-21 exerted about 30–35 % inhibition of MCF-7 proliferative activity in 48 h (Fig. S31A). Whereas, in A-549 cells, the antiproliferative effect of miR-21-targeted aRNases accounted to 50 % after the same period, but was on the border of statistically-significant differences from the control Crab-α-Scr conjugate (Fig. S31A). The proliferative activity of B16 cells remained almost unchanged in response to incubation with "Crab" aRNases. The different sensitivities of cells to aRNases may be associated with differences in the initial proliferation rate of cell lines, as well as with differences in intracellular localization and trafficking in certain cell types.

The study of the influence of miRNA-targeted "Crab" RNases on the viability of normal cells revealed that the conjugates have negligible effects on the survival of untransformed human fibroblast cells hFF3 (Fig. S31B). Previous studies also provided evidence of the selective inhibitory action of anti-miR-21 therapy specifically towards tumor cells, without eliciting comparable effects on normal cells [77].

WST data on the antiproliferative effect of "Crab" aRNases in MCF-7 and A-549 cells were supported by xCELLigence Real-Time Cell Analysis. Monitoring of cell growth showed that Crab-α-21, Crab-β-21 and Crab-p-21 exerted approximately 45–55 % suppression of MCF-7 cell growth (Fig. 6F and G). In contrast, the control (Crab-α-Scr) did not exert any negative effect on the proliferation of MCF-7 cells. The antiproliferative effect of Crab-α-21 and Crab-β-21 was even greater in A-549 cells, which showed a remarkable suppression of cell growth by approximately 85 %. However, the antiproliferative effect of the control conjugate Crab-α-Scr was also significant (Fig. 6I), thus suggesting that A-549 cells appear to be quite sensitive to "Crab" aRNases. xCELLigence analysis revealed that Crab-α-17 was also rather efficient in suppressing MCF-7 cells growth, causing 40 % decrease in cell growth rate (Fig. 6H). Taken together, these findings indicate that, for certain types of tumor cells, targeted depletion of miR-21 and miR-17 by "Crab" aRNases is beneficial to impair the pro-oncogenic proliferative pathways promoting uncontrolled cell growth.

3.8. Antitumor activity of "Crab" aRNases

The ability of "Crab" aRNases to inhibit tumor growth was studied in the MCF-7 xenograft model in mice. In these experiments, we also considered any correlations between the ribonuclease activity of "Crab" conjugates, including the degree and rate of target miRNA downregulation, and their impact on tumor growth. To this end, we chose the most catalytically-potent Crab-p-21 and less active Crab-α-21 aRNase. In order to assess the genuine antitumor effect and eliminate the influence of potentially imperfect methods of *in vivo* targeted delivery, we employed a simplified experimental scheme by bypassing direct administration and, instead, introducing aRNases/Lipofectamine™ 2000 complexes into mice within xenogeneic tumor cells. To achieve that, MCF-7 tumor cells were transfected with aRNases *in vitro* using Lipofectamine™ 2000. Subsequently, the transfected cells were implanted into nude mice to monitor tumor growth. The efficacy of treatment with miRNA-targeted "Crab" aRNase was compared with

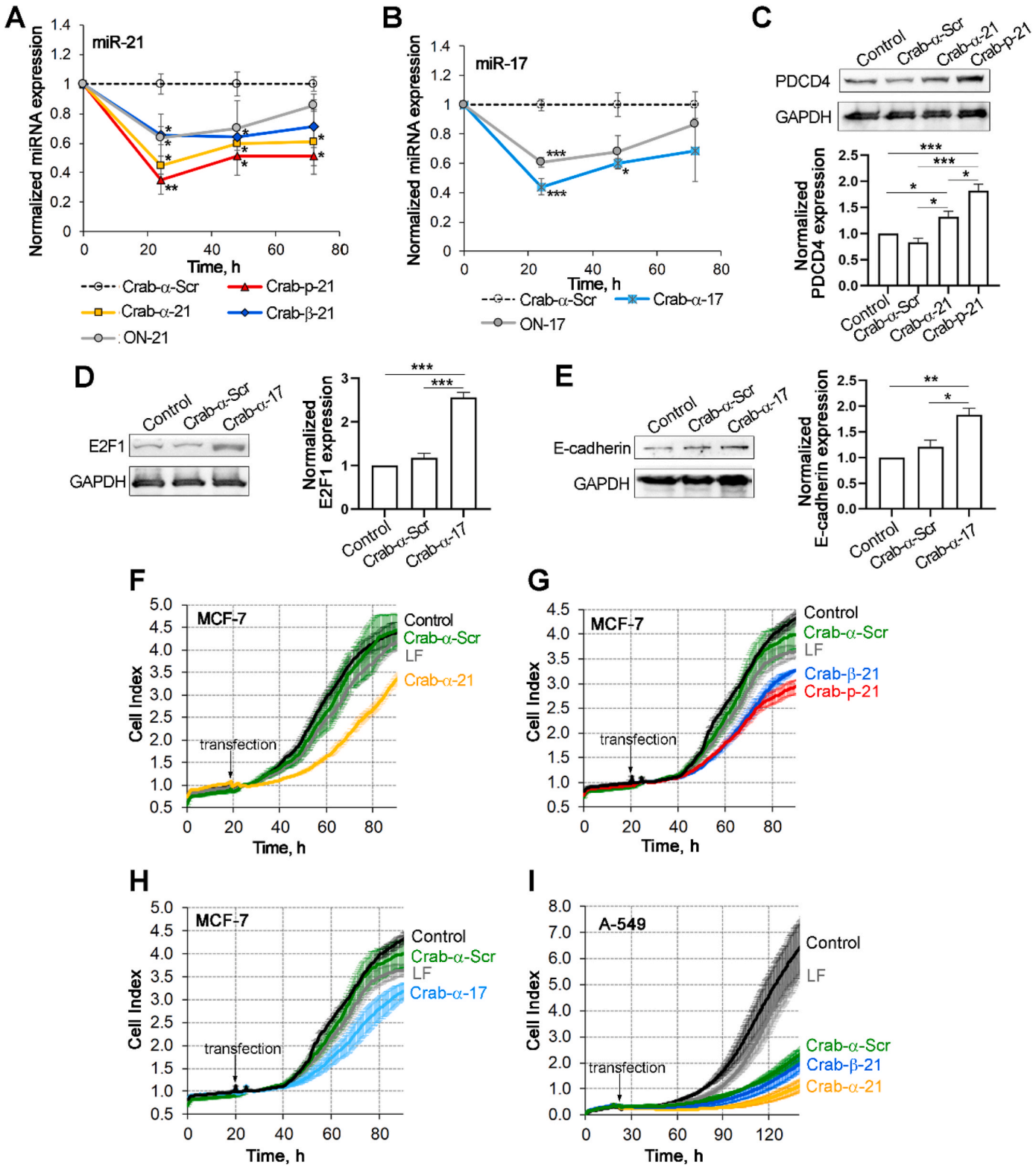

Fig. 6. Biological activity of "Crab" aRNases in tumor cells. (**A, B**) Kinetics of miR-21 downregulation in MCF-7 cells by Crab-p-21, Crab-α-21 and Crab-β-21 aRNases and ON-21 oligonucleotide (**A**), and miR-17 downregulation in MCF-7 cells by Crab-α-17 aRNase and ON-17 oligonucleotide (**B**). Stem-loop PCR data of miR-21 and miR-17 levels are shown. The inhibitory effect of specific "Crab" aRNases was compared to the control non-targeted Crab-α-Scr conjugate. The expression of miRNAs was normalized to U6. Data represent the mean ± s.e. of three independent experiments. *, ** and *** statistically significant differences from control Crab-α-Scr conjugate with $p \leq 0.05$, $p \leq 0.01$ and $p \leq 0.001$. (**C-E**) Western-blot analysis of PDCD4 (**C**), E2F1 (**D**) and E-cadherin (**E**) protein level 72 h after transfection of MCF-7 cells by Crab-α-21, Crab-p-21 (**C**) and Crab-α-17 (**D, E**). Protein levels were normalized to the level of GAPDH. Data represent the mean ± s.e. of three independent experiments. *, ** and *** statistically significant differences with $p \leq 0.05$, $p \leq 0.01$ and $p \leq 0.001$. (**F-H**) Real-time analysis of the growth rate of MCF-7 cells after transfection with Crab-α-21 (**F**), Crab-β-21, Crab-p-21 (**G**) and Crab-α-17 (**H**) aRNases. (**I**) Real-time analysis of the growth rate of A-549 cells after transfection with Crab-α-21 and Crab-β-21. Control – tumor cells without treatment. LF – tumor cells treated with Lipofectamine™ 2000 only. Cell transfection was performed using Lipofectamine™ 2000 with aRNase concentration of 1 μM.

control groups, in which mice were injected either with intact MCF-7 cells or with cells pretreated with the non-specific Crab-α-Scr conjugate. Analysis of tumor growth kinetics showed (Fig. 7A, B) that Crab-p-21 demonstrated the most profound antitumor effect by inhibiting tumor growth by 85 % as compared to that of the control Crab-α-Scr conjugate. The less catalytically-active Crab-α-21 also appeared less effective *in vivo*, but still showed ≈50 % retardation of tumor growth, as compared with non-specific Crab-α-Scr. Data pointed to a direct correlation between the different "Crab" ribonuclease activities and their antitumor effect, indicating scaling between the strong antitumor effect of Crab-p-

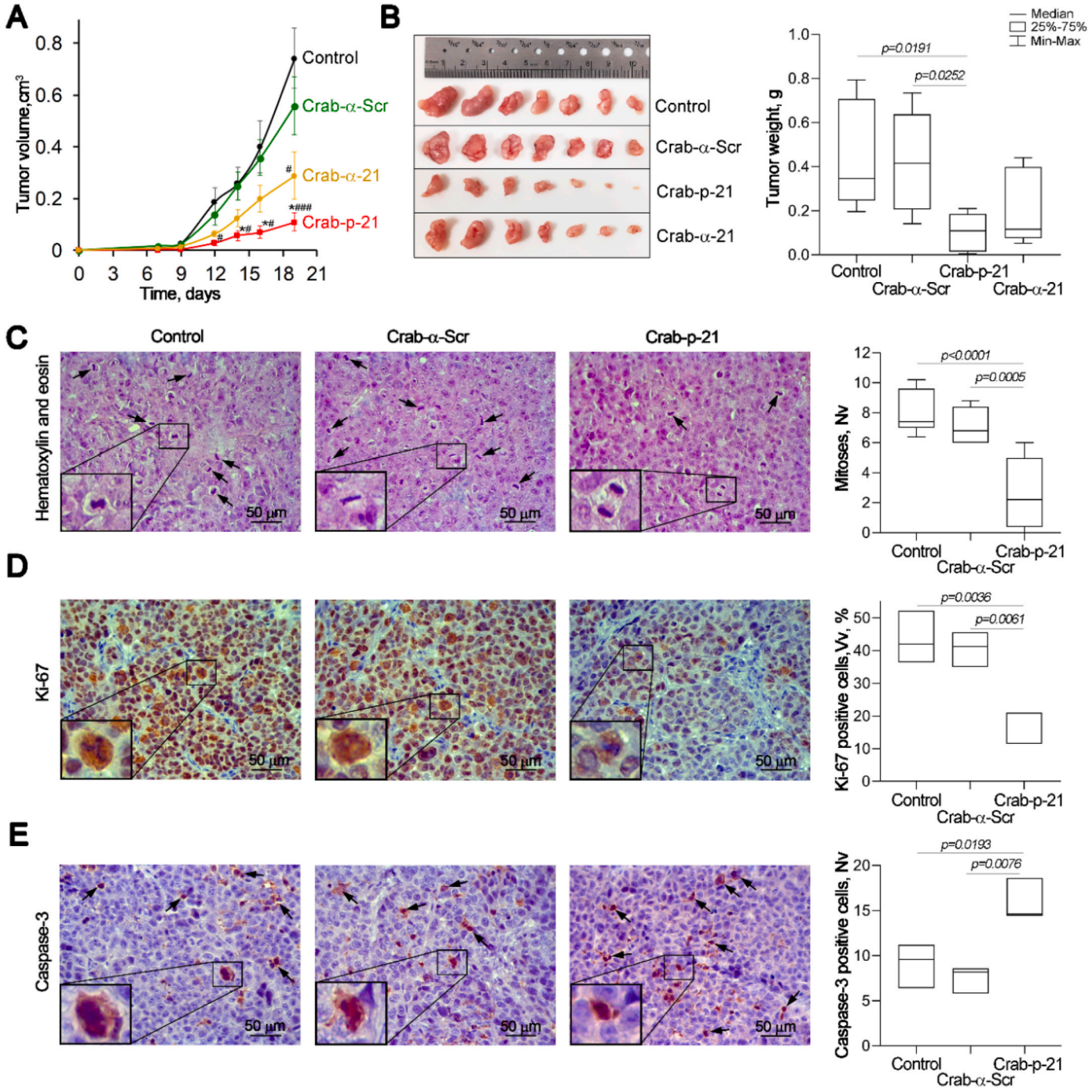

Fig. 7. Antitumor effect of miR-21-targeted "Crab" aRNases in breast carcinoma MCF-7 model. MCF-7 cells were transfected *in vitro* with Crab-p-21, Crab-α-21 and Crab-α-Scr (1 μM) using Lipofectamine™ 2000 followed by subcutaneous implantation in nude mice (n = 7). **(A)** Dynamics of MCF-7 tumor growth. Control – mice injected with intact MCF-7. *– statistically-significant differences from Crab-α-Scr with $p \leq 0.05$. $^{\#}$ and $^{\#\#\#}$ – statistically significance from Control with $p \leq 0.05$ and $p \leq 0.001$. **(B)** Tumor weight on day 19 after implantation. **(C)** Typical images of tumor sections after hematoxylin and eosin staining and morphometric analysis of tumor tissue with mitosis counting. Mitoses are indicated by arrows. Typical examples of individual mitotic events are shown in the bottom left corner. **(D, E)** Typical images of tumor sections after immunohistochemical staining with Ki-67 (**D**) and caspase-3 (**E**) primary antibodies. Typical examples of Ki-67 and caspase-3 positive cells are shown in the bottom left corner. Left panels in **D** and **E** show Ki-67 and caspase-3 positive cell counting, respectively. All images are shown at magnification × 400. Bar corresponds to 50 μm. Nv, the numerical density indicating the number of particles in the unit tissue volume. Vv %, the volume density representing the volume fraction of tissue occupied by the studied compartment. Data were statistically analyzed using one-way ANOVA with a post hoc Tukey test; p value indicates a statistically-reliable difference.

21 and its high catalytic activity. Based on these findings, further histological analysis of proliferative and pro-apoptotic activity of tumor tissue was focused on the effects of Crab-p-21.

Morphometric analysis of hematoxylin and eosin staining of tumor sections showed that Crab-p-21 significantly reduced mitotic activity of MCF-7 tumors, providing 3-fold decrease in the numerical density of mitoses in tumors, in comparison with Crab-α-Scr (Fig. 7C). Experimental data indicate a positive correlation between miR-21 expression and the level of Ki-67, a proliferation marker widely used in clinical studies, which points to the active proliferative phase in tumor growth [78]. Immunohistochemical staining of MCF-7 xenografts with Ki-67-specific antibodies demonstrated that, in the control and Crab-α-Scr groups, approximately 40 % of tumor cells were Ki-67-positive (Fig. 7D). Treatment of tumor cells with Crab-p-21 resulted in a decrease in the number of Ki-67-positive cells in transplanted tumors by up to 12 %, indicating that a more than 3-fold decrease in the proliferative activity of tumor cells *in vivo* was achieved, fully aligned with effects on mitotic activity of tumors (Fig. 7D). The antiproliferative activity of "Crab" aRNases shown in cultured tumor cells translated into a tumor model in mice.

miR-21 is known to be involved in negative regulation of the caspase-3 apoptotic pathway [74]. Morphometric analysis of caspase-3 immunohistochemical images demonstrated that tumor tissue in the control and Crab-α-Scr groups is characterized by a low level of apoptotic activity (Fig. 7E). Treatment of cells with Crab-p-21 led to 1.5-fold increase in an average number of caspase-3-positive cells, testifying to the increased pro-apoptotic activity of tumor tissue in response to miR-21-targeted treatment (Fig. 7E). Targeted downregulation of miR-21 in tumor cells by specific "Crab" aRNases contributed to inhibition in their proliferative potency and an increase in pro-apoptotic activity, which translated into retardation of tumor growth in mice.

The extended antitumor efficacy exhibited by the developed "Crab" aRNases relies on several important factors, such as (i) the inherent catalytic ribonuclease activity of "Crab" aRNases, which (ii) can be reenforced further through synergy with RNase H, (iii) their enhanced stability in biological environments, and (iv) the selection of the functionally-significant miRNA target – miR-21. miR-21 is recognized as a powerful multifunctional oncogene, which is considered as a therapeutic target in many anti-cancer preclinical studies [74,79]. The efficient suppression of miR-21 by Crab-p-21, even with a single application, led to substantial reorganization of cellular signaling pathways, resulting in significant inhibition of its mainline malignant properties.

4. Discussion

For a variety of key biological functions (*e.g.,* defense, gene silencing, translational repression, RNA maturation, processing, expression control, DNA replication and repair) nature often relies on actions of nucleolytic enzymes, which are not sequence-specific *per se*, although might be either base- or site-specific. In order to gain accuracy in recognition and catalysis, some natural endonucleases (*e.g.,* RISC-AGO2, RNase H, CRISPR-Cas) recruit separate RNA or DNA guide sequences and rely upon precision of Watson-Crick base-pairing between guide strands and target nucleic acids. However, the high level of sequence-specificity comes with a price: the high thermodynamic stability required for absolute sequence-specificity often becomes a major barrier in gaining the reaction catalytic turnover, because it opposes the ability of such enzyme complexes to leave the biotarget after each enzymatic event. Here, we overcame this thermodynamic barrier in a different way by using new synthetic artificial RNase, which has no biological analogues, but which became highly synergistic when working together with the natural endonuclease, RNase H. The simultaneous action of "Crab" aRNases and RNase H at their different mechanistic locations of the target regulatory RNA molecules, miR-21 and miR-17, led to a manifold synergy in their catalytic action, demonstrated here.

As evident from our experimental data and mathematical modeling, the likely mechanism of this synergistic "Crab"-like pincer attack is based on harnessing the dynamics of the heteroduplex to attack bonds in the complementary RNA region, when it periodically becomes single-stranded, thus destabilizing the heteroduplex by cleavage and allowing entropy to overcome the remaining thermodynamic barrier. Both the core 1:1 complex and 2:1 assembly of RNA with the "Crab" aRNase are dynamic supramolecular structures. The likelihood of catalytic attacks was indicated by peptide dynamic modeling studies (Fig. 2), both at the pair of dangling single strands of RNA in 2:1 assemblies, which offer for attack prolonged stretches of the exposed RNA strands, and at the edges of the heteroduplex during sporadic fraying of the double-stranded heteroduplex at its edges. Such attacks likely allowed the "Crab" arrangement of catalytic peptides to destabilize the heteroduplexes through cleavage and promote turnover. Although the dangling single RNA strands of 2:1 assemblies would not be hybridized when cleaved, the other parts of each of the two RNA strands would be in the heteroduplex. Consequently, just like cleavage at the edge region of the heteroduplex, loss of parts of the complementary region would leave gaps, which would allow intact RNA to bind, outcompete and displace any cleaved fragment remaining hybridized. Such gaps are well established in oligonucleotide binding cascades in molecular machines to provide toeholds for competitive displacement by a longer incoming strand, where the velocity of displacement increases with the length of the toehold, up to 5–6 nucleotide base pairs [54,55]. Here, rather than including toeholds for binding, equivalent toeholds were created in the hybridized miRNA sequences by catalytic cleavage following the attack from the sequence-specific "Crab"-type aRNases. Despite rapid cleavage of 5'-[^{32}P]-labeled fragments, cleavage in the heteroduplex regions was apparent (Fig. 3 and Fig. S9) for both miR-21 (at U5-U6 and particularly at U6-A7 and C9-A10 positions) and for miR-17 (at U6-G7 and particularly at U10-A11 and C12-A13 positions). Additional cleavage elsewhere was visible only at the 3′-terminus of miRNA (particularly, at G21-A22 in miR-21, and at U21-A22 in miR-17), but with an apparent lesser extent. We anticipate that cleavage within the heteroduplex is even more advantageous under multiple turnover conditions, where dangling single strands in 2:1 assemblies can provide additional opportunities for multiple cuts to encourage competition from intact miRNA sequences, promote fragment displacement and liberate aRNases for the next catalytic cycle. Under single turnover conditions though, the cleavage within the heteroduplex (Fig. S9) can only be achieved through edge-fraying dynamics of the 1:1 assembly, which could have been responsible for opening the ends of the heteroduplex for catalytic attack.

We investigated whether the experimentally-observed cleavage could be considered as a function of the probability of in-line R-R attack of each bond in our mathematical model of the "Crab" aRNase and the specificity of cleavage of each bond when attacked, throughout the progress of the *single* and *multiple turnover* reaction conditions. Despite the wide range of data and extent of change considered, specificities estimated for cleavage of bonds with the same base neighbors were of similar order for the same bonds in different miRNA sequences and locations, at least for the early stages of reaction progress dominated by primary cleavage events, suggesting a reasonable first approximation (Fig. 4). Specificities for the most sensitive pyrimidine-A bonds were up to 2 orders of magnitude greater than purine-X bonds. Armed with the cleavage specificity of each bond, the relative contributions of cleavage at the heteroduplex edges and in dangling single strands were analyzed to estimate these contributions to the mechanism of aRNase turnover, during the progress of cleavage reactions (Fig. 4).

The Crab-p-21 design exhibited the highest ribonuclease activity amongst all investigated structural variants of miR-21-specific aRNases here and outperformed the catalytic properties of the earlier reported, most-active "hairpin" peptidyl-oligonucleotide conjugate against miR-21 [36]. Interestingly, in the presence of a high (relative to physiological) concentration of $MgCl_2$ (8 mM), cleavage efficiency was reduced

(Fig. S24), presumably due to the duplex stabilizing effect of Mg^{2+} ions, which may also reduce the ability of the cleaved RNA products to leave the conjugates and initiate the next cleavage cycle. Nonetheless, even under these conditions, the "Crab" aRNase retained the ability to cleave RNA present in excess.

The "Crab" aRNase design provided a further advantage by forming a continuous region of *RNA:DNA* heteroduplex, which served as a substrate for RNase H to perform additional cleavage at the central bulge and 3′-supplementary interaction regions of miRNA, less attacked by the "Crab" aRNase, thus offering additional biological benefits. The enormous additional synergy from the joint action of these artificial and natural enzymes may be attributed to their *positional* differences in attack of the heteroduplex, which was mutually beneficial for both enzymes. Indeed, rapid turnover of the "Crab" aRNase could be facilitated by extra cleavage events catalyzed by RNase H in the central part of the hybridized complex with miRNA, which would unavoidably reduce the size of the cleaved fragments and encourage their rapid release. Reciprocally, the stalled turnover of RNase H guided by catalytically-inactive antisense oligonucleotide (which was evident at lower concentration of RNase H working alone), was overcome with the assistance from "Crab" aRNase, when enzymic turnover was dramatically increased (Fig. 5). Presumably, the demolition of the 5′-end of the heteroduplex by "Crab" aRNases (evident from Figs. 3 and 5), which serves as a loading site for RNase H, facilitates its release from the "damaged" complex to allow the next attack (alone or jointly with "Crab" aRNase) on the fresh miRNA sequence.

According to the accepted mechanism of miRNA function [45,46], AGO2 MID domain recognizes the 5′-end of mature miRNA, further clamped at the 3′-end by its PAZ domain, which displays the pre-organized helically-shaped "seed" region for efficient search for complementary mRNA sequences. In addition, Ago2 exposes the 3′-supplementary interaction region of miRNA to facilitate subsequent base-paring with the target messenger RNA. Upon translational repression, when miRNA binds to mRNA targets, AGO2 protects miRNA from unintended degradation. In contrast, during the miRNA utilization process, known as Target-Directed MiRNA Degradation (TDMD), a TDMD target binds to miRNA through extended base-pairing, so that the 3′-end of miRNA is released out of the AGO2 PAZ domain, thus making miRNA accessible for enzymatic degradation [80,81]. This can only happen if the significant part of miRNA, spanning across the sequence up to the 17th nucleotide, is involved in base-pairing, when the 3′-end of miRNA becomes pushed out of the PAZ domain to initiate its degradation [47].

Similarly, the accessibility of certain miRNA regions within the *miRNA:AGO2* complex provides an opportunity for aRNases to attack AGO2-protected miRNA in a sequence-specific manner (Fig. 8A). The continuous, uninterrupted hybridized assembly of the "Crab" aRNase with the miRNA central segment, and further regions up to the 17th or

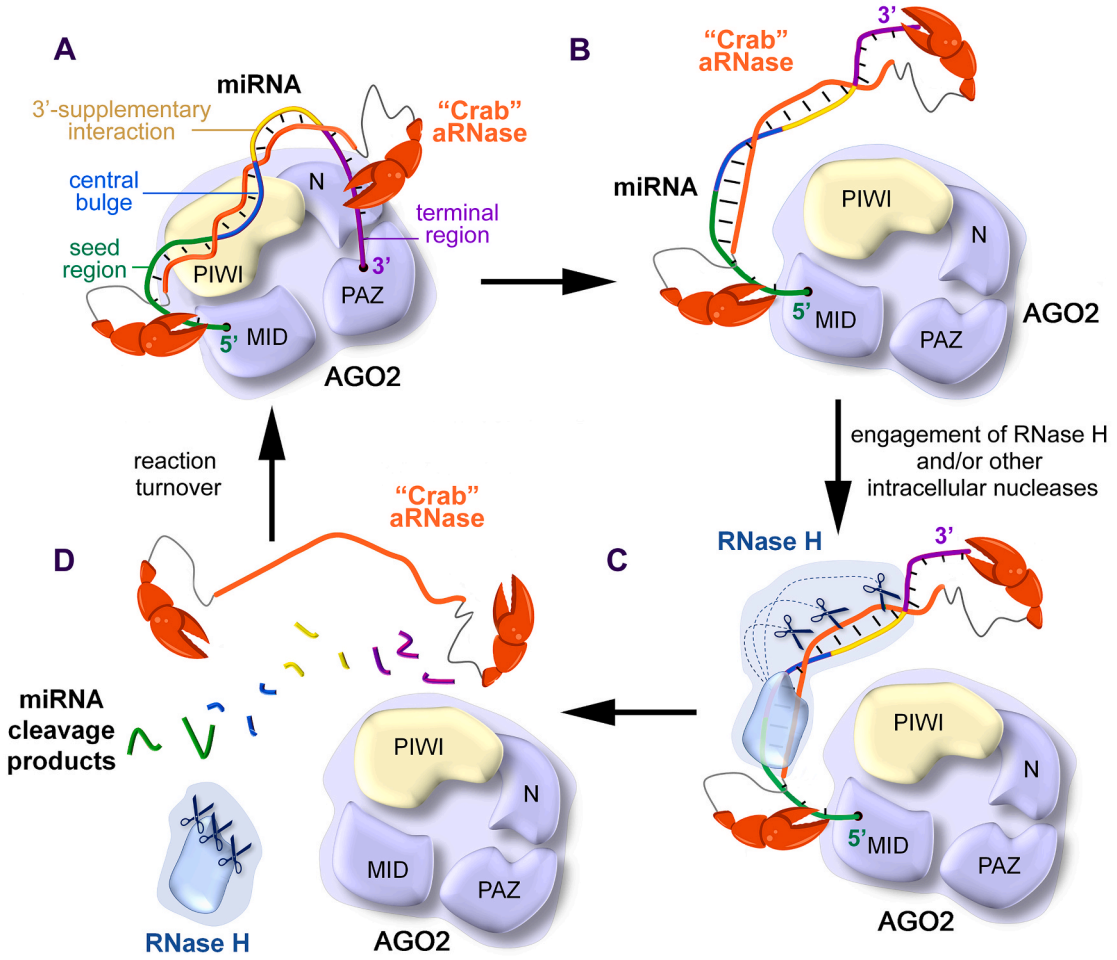

Fig. 8. Schematic illustration of a possible mechanism of miRNA degradation mediated by "Crab" aRNases. (**A**) Model depicting the capture of miRNA by "Crab" aRNase through binding in the central region, while the catalytic peptides attack the seed and terminal regions of miRNA. (**B**) Release of the 3′-end of miRNA from AGO2 PAZ pocket facilitated by 3′-pairing with the "Crab" conjugate, leading to the disruption of AGO2 protection. (**C**) Nuclease attack by "Crab" aRNase, accompanied by recruitment of RNase H and engagement of intracellular nucleases involved in TDMD processes. (**D**) Complete degradation of miRNA at all functionally-significant determinants as a result of the combined nuclease attack.

18th nucleotide (*i.e.*, for miR-21 or miR-17, respectively) may lead to release of the 3′-end of the miRNA, thus making it defenseless against both cellular nucleases as well as aRNase itself (Fig. 8B).

Cleavage experiments showed (Fig. 3 and Fig. S9) that both miR-21 and miR-17-targeted "Crabs" cleaved miRNA at the first phosphodiester bond with high efficiency. It has been reported that the first nucleotide at the 5′-end of the miRNA sequence is not involved in mRNA target recognition and repression, but serves for immobilization of miRNA at the MID domain of AGO2 [45]. Thus, cleavage at the first phosphodiester bond by "Crab" aRNases may destabilize, and even disassociate, the *miRNA:AGO2* complex, thus making miRNA fully accessible for cleavage by "Crab" aRNase and other intracellular nucleases, to become ultimately non-functional for translational repression (Fig. 8C and D).

We also showed that "Crab" aRNases are capable of cleaving miRNAs at their seed region, and the efficiency of cleavage directly depended upon their sequence, in particular, upon the presence of the most sensitive pyrimidine-A bonds. The miR-21 seed region, 5′-AGCUUAUC-3' (with 4 × Pyr and 3 × Pu residues), contains one sensitive bond U6-A7, while miR-17 seed region, 5′-AAAGUGCU-3' (with 2 × Pyr and 5 × Pu residues), is purine-rich and does not contain any pyrimidine-A sites. Instead, the miR-21-targeted "Crabs" exhibited significant cleavage in the miR-21 sequence at the C1-A2 site and in the seed region, particularly at the U6-A7 bond, with weaker cleavage at the G3-C4 and C4-U5 positions (Fig. 3B). The presence of an A-T rich stretch at the 5′-end of the heteroduplex seems to have caused a "fraying" effect [82] originated from an occasional breaking of the hydrogen bonds of the terminal base pairs, thus leading to an exposure and cleavage at the U6-A7 and C9-A10 sites. Cleavage of miR-17 by the specific Crab-α-17 occurred predominantly at the C1-A2 site, as well as 3′-terminal U21-A22 and C17A-18 sites. The "seed" segment appeared cleaved here to a much lesser extent, with only a visible faint cleavage at U6-G7 position (Fig. 3A and B). Cleavage at less-sensitive bonds within the "seed" region may occur, but at much slower rate, masked by cleavage at the more sensitive. Thus, the distinctive cleavage patterns observed here for miR-21 and miR-17 suggest the importance of base specificity of "Crab" aRNases, which ranged over two orders of magnitude for different base neighbors (Fig. 4) and thereby becomes an important factor when designing miRNA-targeted aRNase.

These findings and mathematical model provide valuable insights for the rational design of other effective miRNA therapeutics. The ability of "Crabs" to induce cleavage at the "seed" region, as well as at the 5′-proximal and 3′-terminal phosphodiester bonds, which are responsible for anchoring miRNA in the specialized structural pockets of AGO2, appears to be one of their key advantages, especially in comparison with antisense oligonucleotides lacking any catalytic groups. Such cleavage promotes the detachment of miRNA from its protective association with AGO2, which (1) makes this silencing complex non-functional and (2) exposes miRNA to rapid degradation by cellular nucleases (Fig. 8). This additional advantage offered by "Crabs" in intracellular conditions makes them unique among the other types of aRNases [36,37,48,49].

Our experimental data (Fig. 5A – D) provides strong evidence of the reciprocally-synergistic action of "Crab" aRNases and RNase H to inactivate target miRNAs through cleavage possible at every bond within the *RNA:DNA* hybrid, starting from the 5th nucleotide from the 5′-end of the heteroduplex, thus affecting the central region and the region of 3′-supplementary interactions. We can hypothesize therefore that, in the intracellular environment, even when RNase H is not abundant, the irreversible demolition of all functionally significant miRNA segments becomes feasible, particularly by the joint action of "Crab" aRNase and RNase H (Fig. 8C and D). Alongside this, the hybridization of miRNA with the "perfect match" oligonucleotide recognition domain of "Crab" aRNase can mimic the binding of miRNA to its decay targets [46,80] and thus independently induce natural intrinsic mechanisms of miRNA utilization, including recruitment of other intracellular nucleases as well as 3′-trimming and tailing, which accompanies TDMD. In cells and tissues, such combined action of the exogeneous (synthetic) aRNase and intracellular (natural) nucleases, could trigger degradation of the miRNA sequence into short 1–2 nucleotide fragments, thus leading to the complete loss of miRNA functionality. This process may have profound implications on miRNA-associated cell signaling cascades and ultimately lead to a disruption of their regulatory roles within the cell, which was evident here from our experiments with the cancer cell lines (Fig. 6) and studies in mouse tumor models (Fig. 7).

The study of the biological effect of "Crab" aRNases demonstrated a clear relationship between catalytic activity of Crab-p-21 aRNase and its biological miRNA inhibitory effect. miRNAs exhibit remarkably rapid production rates in both proliferative and non-proliferative cells. Notably, the highly-abundant miR-21, particularly in oncotransformed cells, was found to be synthesized at an impressive rate of 110 ± 50 copies/cell/min [35]. Even at a production rate 10-times lower (*e.g.* 10 copies/cell/min), miR-21 would still be synthesized faster than the most rapidly produced mRNA and pre-rRNA counterparts [83,84]. Considering the extraordinary rate of intracellular miRNA synthesis and the abundance of oncogenic miRNAs in cells, the observed reduction in target miRNA levels mediated by miR-21-specific "Crab" aRNase demonstrated a high efficacy of silencing. Interestingly, despite the lower *in vitro* ribonuclease activity of Crab-α-21 against synthetic miR-21 (Fig. 3), its inhibitory effect in tumor cell lines approached the effect of Crab-p-21 and sometimes exceeded that from Crab-β-21 (Fig. 6). The latter might be explained by greater nuclease resistance and thus longer lifetime of the alpha isomer as compared with the natural beta isomer of Crab-β-21, but the role of some other contributing factors should not be ignored.

In cell culture experiments, both miR-21 and miR-17 specific conjugates exhibited notable antiproliferative activity. However, the observed effects varied among different cell lines, thus suggesting the potential influence of factors such as the initial proliferation rate, intracellular localization, and trafficking of aRNases, through perhaps less variations in the intracellular abundance and activity of RNase H. The complex interplay between these factors and the efficacy of miRNA-targeted conjugates, highlights the need for further investigations to fully elucidate and optimize their performance, not least their cellular delivery in different cellular contexts.

The overall biological effects of "Crab" aRNases are *on par* with or surpass those of existing miR-21 oligonucleotide inhibitors. Typically, miR-21-targeted oligonucleotide inhibitors, including commercial inhibitors, LNA-modified oligonucleotides, and synthetic circular RNAs can achieve a reduction of miR-21 levels in tumor cells ranging from 50 % to 80 % and inhibition of cell growth by 20–50 % [32,85–88]. The "Crab" aRNase reported here sequence-specifically reduced the miR-21 level by 65 % and showed the inhibition of cell growth by 30–55 % when administered at catalytic levels - at much less than stochiometric dose and likely requiring catalytic turnover.

A single treatment of MCF-7 tumor cells with the most catalytically-active Crab-p-21 prior to transplantation into mice led to 85 % reduction in primary tumor volume. The observed correlation between ribonuclease activity, downregulation of miR-21, and the antitumor effect supports the notion that the catalytic properties *per se* of "Crab" aRNases play a crucial role in their efficacy. The lack of chemical modifications provides additional benefit for synergistic recruitment of RNase H in intracellular environment, although additional protection with RNase H compatible modifications [15–17] can be considered in the future.

Targeting pathophysiological processes with catalytically-active miRNA silencers, provenly synergistic with RNase H, offers a promising approach for further development, particularly to address the need for lower dosing and greater persistence after dosing, where imperfect delivery of silencing and conventional therapies fail treatment of severe diseases.

5. Conclusions

aRNases were developed with pairs of highly-flexible catalytic

peptides, positioned each side of an RNA recognition motif for synergistic pincer attack of phosphodiester bonds along the length of each face of the heteroduplexes formed upon sequence-specific capture of miRNA. These "Crab"-like aRNases:

a) attacked the heteroduplex region, consistent with fraying of duplex edges and dangling strands of competing miRNA molecules, from the probabilities of in-line attack of bonds by pairs of arginine residues, approximated by dynamic modeling;
b) exhibited high specificities for bond cleavage with pyrimidine–A base neighbors, estimated as over two orders of magnitude greater than bonds with other base neighbors, when cleavage patterns were modulated by the probabilities of in-line attack of each bond;
c) cleaved particularly the 5′-part of heteroduplexes, which would offer toeholds for binding of intact miRNA to facilitate competitive displacement of longer fragments necessary for the catalytic turnover observed;
d) which also cleaved the loading region of RNase H, to destabilize the whole heteroduplex, likely facilitating the synergistic RNase H turnover;
e) provided synergy with RNase H by demolishing all functional regions of miRNA;
f) achieved 65 % knock-down of miR-21, one of the most rapidly produced, when administered well below stoichiometric levels, requiring multiple turnover;
g) demonstrated 85 % reduction in primary tumor volume in mice, with a clear relationship between catalytic activity and therapeutic miRNA inhibitory effect.

License statement

Data access statement

All data supporting this study are provided as Supplementary information (**Appendix A**) accompanying this paper at https://doi.org/10.1016/j.biomaterials.2024.122604.

CRediT authorship contribution statement

Daria Chiglintseva: Writing – original draft, Visualization, Investigation, Formal analysis. **David J. Clarke:** Writing – review & editing, Writing – original draft, Visualization, Investigation, Formal analysis, Conceptualization. **Aleksandra Sen'kova:** Methodology, Investigation. **Thomas Heyman:** Investigation. **Svetlana Miroshnichenko:** Investigation, Formal analysis. **Fangzhou Shan:** Investigation. **Valentin Vlassov:** Writing – review & editing, Supervision, Funding acquisition. **Marina Zenkova:** Writing – review & editing, Writing – original draft, Supervision, Funding acquisition, Conceptualization. **Olga Patutina:** Writing – review & editing, Writing – original draft, Supervision, Project administration, Investigation, Formal analysis, Conceptualization. **Elena Bichenkova:** Writing – review & editing, Writing – original draft, Supervision, Project administration, Investigation, Funding acquisition, Conceptualization.

Declaration of competing interest

The authors declare that they have no known competing financial interests or personal relationships that could have appeared to influence the work reported in this paper.

Data availability

Data will be made available on request.

Acknowledgements

This work was supported by Russian Science Foundation (grant number: 19-14-00250), Russian State funded budget project of ICBFM SB RAS # 121031300044–5; and by the Biotechnology and Biological Sciences Research Council [BB/K012622/1], Engineering and Physical Sciences Research Council [EP/E003400/1, EP/G03737X/1], and Medical Research Council [MR/N013751/1] before collaborative support was curtailed in 2022.

We express our gratitude to the Laboratory of Medicinal Chemistry at the ICBFM SB RAS for synthesis of the oligonucleotide analogues. Special thanks are extended to Dr. Maria I. Meschaninova for RNA synthesis. Additionally, we would like to extend our gratitude to Dr. Alexander Chernonosov and Dr. Svetlana Baranova from the Centre of Collective Use at the ICBFM SB RAS for their assistance with the Mass Spectrometry analysis of the conjugates. Lastly, we would like to acknowledge the technical support provided by Neil O'Hara and Albina Vladimirova.

Appendix A. Supplementary data

Supplementary data to this article can be found online at https://doi.org/10.1016/j.biomaterials.2024.122604.

References

[1] J. O'Brien, H. Hayder, Y. Zayed, C. Peng, Overview of MicroRNA biogenesis, mechanisms of actions, and circulation, Front. Endocrinol. 9 (2018), https://doi.org/10.3389/fendo.2018.00402.
[2] K. Saliminejad, H.R. Khorram Khorshid, S. Soleymani Fard, S.H. Ghaffari, An overview of microRNAs: biology, functions, therapeutics, and analysis methods, J. Cell. Physiol. 234 (2019) 5451–5465, https://doi.org/10.1002/jcp.27486.
[3] S.M. Hammond, An overview of microRNAs, Adv. Drug Deliv. Rev. 87 (2015) 3–14, https://doi.org/10.1016/j.addr.2015.05.001.
[4] R. Rupaimoole, F.J. Slack, MicroRNA therapeutics: towards a new era for the management of cancer and other diseases, Nat. Rev. Drug Discov. 16 (2017) 203–221, https://doi.org/10.1038/nrd.2016.246.
[5] J. Inoue, J. Inazawa, Cancer-associated miRNAs and their therapeutic potential, J. Hum. Genet. 66 (2021) 937–945, https://doi.org/10.1038/s10038-021-00938-6.
[6] S. Zhou, J. Jin, J. Wang, Z. Zhang, J.H. Freedman, Y. Zheng, L. Cai, miRNAS in cardiovascular diseases: potential biomarkers, therapeutic targets and challenges, Acta Pharmacol. Sin. 39 (2018) 1073–1084, https://doi.org/10.1038/aps.2018.30.
[7] L. Leggio, S. Vivarelli, F. L'Episcopo, C. Tirolo, S. Caniglia, N. Testa, B. Marchetti, N. Iraci, microRNAs in Parkinson's disease: from pathogenesis to novel diagnostic and therapeutic approaches, Int. J. Mol. Sci. 18 (2017) 2698, https://doi.org/10.3390/ijms18122698.
[8] C.A. Juźwik, S.S. Drake, Y. Zhang, N. Paradis-Isler, A. Sylvester, A. Amar-Zifkin, C. Douglas, B. Morquette, C.S. Moore, A.E. Fournier, microRNA dysregulation in neurodegenerative diseases: a systematic review, Prog. Neurobiol. 182 (2019) 101664, https://doi.org/10.1016/j.pneurobio.2019.101664.
[9] K. Chandan, M. Gupta, M. Sarwat, Role of host and pathogen-derived MicroRNAs in immune regulation during infectious and inflammatory diseases, Front. Immunol. 10 (2020), https://doi.org/10.3389/fimmu.2019.03081.
[10] F. Angelucci, K. Cechova, M. Valis, K. Kuca, B. Zhang, J. Hort, MicroRNAs in alzheimer's disease: diagnostic markers or therapeutic agents? Front. Pharmacol. 10 (2019) https://doi.org/10.3389/fphar.2019.00665.
[11] G. Casi, D. Neri, Antibody–drug conjugates and small molecule–drug conjugates: opportunities and challenges for the development of selective anticancer cytotoxic agents, J. Med. Chem. 58 (2015) 8751–8761, https://doi.org/10.1021/acs.jmedchem.5b00457.
[12] J.W. Scannell, A. Blanckley, H. Boldon, B. Warrington, Diagnosing the decline in pharmaceutical R& D efficiency, Nat. Rev. Drug Discov. 11 (2012) 191–200, https://doi.org/10.1038/nrd3681.
[13] H. Chang, B. Yi, R. Ma, X. Zhang, H. Zhao, Y. Xi, CRISPR/cas9, a novel genomic tool to knock down microRNA in vitro and in vivo, Sci. Rep. 6 (2016) 22312, https://doi.org/10.1038/srep22312.
[14] J. Yang, X. Meng, J. Pan, N. Jiang, C. Zhou, Z. Wu, Z. Gong, CRISPR/Cas9-mediated noncoding RNA editing in human cancers, RNA Biol. 15 (2018) 35–43, https://doi.org/10.1080/15476286.2017.1391443.
[15] S.K. Miroshnichenko, O.A. Patutina, E.A. Burakova, B.P. Chelobanov, A.A. Fokina, V.V. Vlassov, S. Altman, M.A. Zenkova, D.A. Stetsenko, Mesyl phosphoramidate antisense oligonucleotides as an alternative to phosphorothioates with improved

biochemical and biological properties, Proc. Natl. Acad. Sci. USA 116 (2019) 1229–1234, https://doi.org/10.1073/pnas.1813376116.
[16] O.A. Patutina, S.K. Gaponova (Miroshnichenko), A.V. Sen'kova, I.A. Savin, D. V. Gladkikh, E.A. Burakova, A.A. Fokina, M.A. Maslov, E.V. Shmendel, M.J. A. Wood, V.V. Vlassov, S. Altman, D.A. Stetsenko, M.A. Zenkova, Mesyl phosphoramidate backbone modified antisense oligonucleotides targeting miR-21 with enhanced in vivo therapeutic potency, Proc. Natl. Acad. Sci. USA 117 (2020) 32370–32379, https://doi.org/10.1073/pnas.2016158117.
[17] S. Gaponova, O. Patutina, A. Sen'kova, E. Burakova, I. Savin, A. Markov, E. Shmendel, M. Maslov, D. Stetsenko, V. Vlassov, M. Zenkova, Single shot vs. Cocktail: a comparison of mono- and combinative application of miRNA-targeted mesyl oligonucleotides for efficient antitumor therapy, Cancers 14 (2022) 4396, https://doi.org/10.3390/cancers14184396.
[18] K.A. Lennox, C.A. Vakulskas, M.A. Behlke, Non-nucleotide modification of anti-miRNA oligonucleotides, Methods Mol. Biol. 1517 (2017) 51–69, https://doi.org/10.1007/978-1-4939-6563-2_3.
[19] A. Boutla, Developmental defects by antisense-mediated inactivation of micro-RNAs 2 and 13 in Drosophila and the identification of putative target genes, Nucleic Acids Res. 31 (2003) 4973–4980, https://doi.org/10.1093/nar/gkg707.
[20] R. Zhang, F. Li, W. Wang, X. Wang, S. Li, J. Liu, The effect of antisense inhibitor of miRNA 106b~25 on the proliferation, invasion, migration, and apoptosis of gastric cancer cell, Tumor Biol. 37 (2016) 10507–10515, https://doi.org/10.1007/s13277-016-4937-x.
[21] S. Zeniya, H. Kuwahara, K. Daizo, A. Watari, M. Kondoh, K. Yoshida-Tanaka, H. Kaburagi, K. Asada, T. Nagata, M. Nagahama, K. Yagi, T. Yokota, Angubindin-1 opens the blood–brain barrier in vivo for delivery of antisense oligonucleotide to the central nervous system, J. Contr. Release 283 (2018) 126–134, https://doi.org/10.1016/j.jconrel.2018.05.010.
[22] J.F. Lima, L. Cerqueira, C. Figueiredo, C. Oliveira, N.F. Azevedo, Anti-miRNA oligonucleotides: a comprehensive guide for design, RNA Biol. 15 (2018) 338–352, https://doi.org/10.1080/15476286.2018.1445959.
[23] S. Miroshnichenko, O. Patutina, Enhanced inhibition of tumorigenesis using combinations of miRNA-targeted therapeutics, Front. Pharmacol. 10 (2019) 1–17, https://doi.org/10.3389/fphar.2019.00488.
[24] M.S. Ebert, J.R. Neilson, P.A. Sharp, MicroRNA sponges: competitive inhibitors of small RNAs in mammalian cells, Nat. Methods 4 (2007) 721–726, https://doi.org/10.1038/nmeth1079.
[25] M.S. Ebert, P.A. Sharp, MicroRNA sponges: progress and possibilities, RNA 16 (2010) 2043–2050, https://doi.org/10.1261/rna.2414110.
[26] A.-L. Liang, T.-T. Zhang, N. Zhou, C.Y. Wu, M.-H. Lin, Y.-J. Liu, miRNA-10b sponge: an anti-breast cancer study in vitro, Oncol. Rep. 35 (2016) 1950–1958, https://doi.org/10.3892/or.2016.4596.
[27] S. Gao, H. Tian, Y. Guo, Y. Li, Z. Guo, X. Zhu, X. Chen, miRNA oligonucleotide and sponge for miRNA-21 inhibition mediated by PEI-PLL in breast cancer therapy, Acta Biomater. 25 (2015) 184–193, https://doi.org/10.1016/j.actbio.2015.07.020.
[28] S. Liu, X. Sun, M. Wang, Y. Hou, Y. Zhan, Y. Jiang, Z. Liu, X. Cao, P. Chen, Z. Liu, X. Chen, Y. Tao, C. Xu, J. Mao, C. Cheng, C. Li, Y. Hu, L. Wang, Y.E. Chin, Y. Shi, U. Siebenlist, X. Zhang, A microRNA 221– and 222–mediated feedback loop maintains constitutive activation of NFκB and STAT3 in colorectal cancer cells, Gastroenterology 147 (2014) 847–859.e11, https://doi.org/10.1053/j.gastro.2014.06.006.
[29] L. Mignacca, E. Saint-Germain, A. Benoit, V. Bourdeau, A. Moro, G. Ferbeyre, Sponges against miR-19 and miR-155 reactivate the p53-Socs1 axis in hematopoietic cancers, Cytokine 82 (2016) 80–86, https://doi.org/10.1016/j.cyto.2016.01.015.
[30] L. Meng, C. Liu, J. Lü, Q. Zhao, S. Deng, G. Wang, J. Qiao, C. Zhang, L. Zhen, Y. Lu, W. Li, Y. Zhang, R.G. Pestell, H. Fan, Y.H. Chen, Z. Liu, Z. Yu, Small RNA zippers lock miRNA molecules and block miRNA function in mammalian cells, Nat. Commun. 8 (2017) 13964, https://doi.org/10.1038/ncomms13964.
[31] S. Müller, A. Wedler, J. Breuer, M. Glaß, N. Bley, M. Lederer, J. Haase, C. Misiak, T. Fuchs, A. Ottmann, T. Schmachtel, L. Shalamova, A. Ewe, A. Aigner, O. Rossbach, S. Hüttelmaier, Synthetic circular miR-21 RNA decoys enhance tumor suppressor expression and impair tumor growth in mice, NAR Cancer 2 (2020) 43–49, https://doi.org/10.1093/narcan/zcaa014.
[32] A.R. Rama, F. Quiñonero, C. Mesas, C. Melguizo, J. Prados, Synthetic circular miR-21 sponge as tool for lung cancer treatment, Int. J. Mol. Sci. 23 (2022) 2963, https://doi.org/10.3390/ijms23062963.
[33] X. Liu, J.M. Abraham, Y. Cheng, Z. Wang, Z. Wang, G. Zhang, H. Ashktorab, D. T. Smoot, R.N. Cole, T.N. Boronina, L.R. DeVine, C.C. Talbot, Z. Liu, S.J. Meltzer, Synthetic circular RNA functions as a miR-21 sponge to suppress gastric carcinoma cell proliferation, Mol. Ther. Nucleic Acids 13 (2018) 312–321, https://doi.org/10.1016/j.omtn.2018.09.010.
[34] C. Diener, A. Keller, E. Meese, Emerging concepts of miRNA therapeutics: from cells to clinic, Trends Genet. 38 (2022) 613–626, https://doi.org/10.1016/j.tig.2022.02.006.
[35] E.R. Kingston, D.P. Bartel, Global analyses of the dynamics of mammalian microRNA metabolism, Genome Res. 29 (2019) 1777–1790, https://doi.org/10.1101/gr.251421.119.
[36] O.A. Patutina, E.V. Bichenkova, S.K. Miroshnichenko, N.L. Mironova, L. T. Trivoluzzi, K.K. Burusco, R.A. Bryce, V.V. Vlassov, M.A. Zenkova, miRNases: novel peptide-oligonucleotide bioconjugates that silence miR-21 in lymphosarcoma cells, Biomaterials 122 (2017) 163–178, https://doi.org/10.1016/j.biomaterials.2017.01.018.
[37] O.A. Patutina, S.K. Miroshnichenko, N.L. Mironova, A.V. Sen'kova, E. V. Bichenkova, D.J. Clarke, V.V. Vlassov, M.A. Zenkova, Catalytic knockdown of miR-21 by artificial Ribonuclease: biological performance in tumor model, Front. Pharmacol. 10 (2019) 1–13, https://doi.org/10.3389/fphar.2019.00879.
[38] O. Patutina, D. Chiglintseva, E. Bichenkova, S. Gaponova, N. Mironova, V. Vlassov, M. Zenkova, Dual miRNases for triple incision of miRNA target: design concept and catalytic performance, Molecules 25 (2020) 1–23, https://doi.org/10.3390/MOLECULES25102459.
[39] O. Patutina, D. Chiglintseva, B. Amirloo, D. Clarke, S. Gaponova, V. Vlassov, E. Bichenkova, M. Zenkova, Bulge-forming miRNases cleave oncogenic miRNAs at the central loop region in a sequence-specific manner, Int. J. Mol. Sci. 23 (2022) 6562, https://doi.org/10.3390/ijms23126562.
[40] Y. Staroseletz, B. Amirloo, A. Williams, A. Lomzov, K.K. Burusco, D.J. Clarke, T. Brown, M.A. Zenkova, E. V Bichenkova, Strict conformational demands of RNA cleavage in bulge-loops created by peptidyl-oligonucleotide conjugates, Nucleic Acids Res. 48 (2020) 10662–10679, https://doi.org/10.1093/nar/gkaa780.
[41] B. Amirloo, Y. Staroseletz, S. Yousaf, D.J. Clarke, T. Brown, H. Aojula, M. A. Zenkova, E. V Bichenkova, "Bind, cleave and leave": multiple turnover catalysis of RNA cleavage by bulge–loop inducing supramolecular conjugates, Nucleic Acids Res. 50 (2022) 651–673, https://doi.org/10.1093/nar/gkab1273.
[42] A. Williams, Y. Staroseletz, M.A. Zenkova, L. Jeannin, H. Aojula, E.V. Bichenkova, Peptidyl-oligonucleotide conjugates demonstrate efficient cleavage of RNA in a sequence-specific manner, Bioconjugate Chem. 26 (2015) 1129–1143, https://doi.org/10.1021/acs.bioconjchem.5b00193.
[43] O.A. Patutina, M.A. Bazhenov, S.K. Miroshnichenko, N.L. Mironova, D.V. Pyshnyi, V.V. Vlassov, M.A. Zenkova, Peptide-oligonucleotide conjugates exhibiting pyrimidine-X cleavage specificity efficiently silence miRNA target acting synergistically with RNase H, Sci. Rep. 8 (2018) 1–15, https://doi.org/10.1038/s41598-018-33331-z.
[44] W.R. Becker, B. Ober-Reynolds, K. Jouravleva, S.M. Jolly, P.D. Zamore, W. J. Greenleaf, High-throughput analysis reveals rules for target RNA binding and cleavage by AGO2, Mol. Cell. 75 (2019) 741–755.e11, https://doi.org/10.1016/j.molcel.2019.06.012.
[45] D.P. Bartel, Metazoan MicroRNAs, Cell 173 (2018) 20–51, https://doi.org/10.1016/j.cell.2018.03.006.
[46] P. Pawlica, J. Sheu-Gruttadauria, I.J. MacRae, J.A. Steitz, How complementary targets expose the microRNA 3′ end for tailing and trimming during target-directed microRNA degradation, Cold Spring Harbor Symp. Quant. Biol. 84 (2019) 179–183, https://doi.org/10.1101/sqb.2019.84.039321.
[47] K. Nakanishi, Anatomy of four human Argonaute proteins, Nucleic Acids Res. 50 (2022) 6618–6638, https://doi.org/10.1093/nar/gkac519.
[48] S. Obad, C.O. dos Santos, A. Petri, M. Heidenblad, O. Broom, C. Ruse, C. Fu, M. Lindow, J. Stenvang, E.M. Straarup, H.F. Hansen, T. Koch, D. Pappin, G. J. Hannon, S. Kauppinen, Silencing of microRNA families by seed-targeting tiny LNAs, Nat. Genet. 43 (2011) 371–378, https://doi.org/10.1038/ng.786.
[49] C. Staedel, C. Varon, P.H. Nguyen, B. Vialet, L. Chambonnier, B. Rousseau, I. Soubeyran, S. Evrard, F. Couillaud, F. Darfeuille, Inhibition of gastric tumor cell growth using seed-targeting LNA as specific, long-lasting MicroRNA inhibitors, Mol. Ther. Nucleic Acids 4 (2015) e246, https://doi.org/10.1038/mtna.2015.18.
[50] N.L. Mironova, D.V. Pyshnyi, D.V. Shtadler, A.A. Fedorova, V.V. Vlassov, M. A. Zenkova, RNase T1 mimicking artificial ribonuclease, Nucleic Acids Res. 35 (2007) 2356–2367, https://doi.org/10.1093/nar/gkm143.
[51] M. Silberklang, A.M. Gillum, U.L. RajBhandary, Use of in vitro 32P labeling in the sequence analysis of nonradioactive tRNAs, Methods Enzymol. 59 (1979) 58–109.
[52] C. Chen, Real-time quantification of microRNAs by stem-loop RT-PCR, Nucleic Acids Res. 33 (2005) e179, https://doi.org/10.1093/nar/gni178, e179.
[53] E. Varkonyi-Gasic, R.P. Hellens, Quantitative Stem-Loop RT-PCR for Detection of MicroRNAs, 2011, pp. 145–157, https://doi.org/10.1007/978-1-61779-123-9_10.
[54] H. Liu, F. Hong, F. Smith, J. Goertz, T. Ouldridge, M.M. Stevens, H. Yan, P. Šulc, Kinetics of RNA and RNA:DNA hybrid strand displacement, ACS Synth. Biol. 10 (2021) 3066–3073, https://doi.org/10.1021/acssynbio.1c00336.
[55] N. Kundu, B.E. Young, J.T. Sczepanski, Kinetics of heterochiral strand displacement from PNA–DNA heteroduplexes, Nucleic Acids Res. 49 (2021) 6114–6127, https://doi.org/10.1093/nar/gkab499.
[56] L. Baldini, R. Cacciapaglia, A. Casnati, L. Mandolini, R. Salvio, F. Sansone, R. Ungaro, Upper rim guanidinocalix[4]arenes as artificial phosphodiesterases, J. Org. Chem. 77 (2012) 3381–3389, https://doi.org/10.1021/jo300193y.
[57] R. Salvio, A. Casnati, Guanidinium promoted cleavage of phosphoric diesters: kinetic investigations and calculations provide indications on the operating mechanism, J. Org. Chem. 82 (2017) 10461–10469, https://doi.org/10.1021/acs.joc.7b01925.
[58] R. Salvio, L. Mandolini, C. Savelli, Guanidine–guanidinium cooperation in bifunctional artificial phosphodiesterases based on diphenylmethane spacers; gem -dialkyl effect on catalytic efficiency, J. Org. Chem. 78 (2013) 7259–7263, https://doi.org/10.1021/jo401085z.
[59] H. Lönnberg, Structural modifications as tools in mechanistic studies of the cleavage of RNA phosphodiester linkages, Chem. Rec. 22 (2022), https://doi.org/10.1002/tcr.202200141.
[60] R.N. Zuckermann, P.G. Schultz, Site-selective cleavage of structured RNA by a staphylococcal nuclease-DNA hybrid, Proc. Natl. Acad. Sci. USA 86 (1989) 1766–1770, https://doi.org/10.1073/pnas.86.6.1766.
[61] J. Rhim, W. Baek, Y. Seo, J.H. Kim, From molecular mechanisms to therapeutics: understanding MicroRNA-21 in cancer, Cells 11 (2022) 2791, https://doi.org/10.3390/cells11182791.
[62] V. Jazbutyte, T. Thum, MicroRNA-21: from cancer to cardiovascular disease, Curr. Drug Targets 11 (2010) 926–935, https://doi.org/10.2174/138945010791591403.

[63] K.A. O'Donnell, E.A. Wentzel, K.I. Zeller, C.V. Dang, J.T. Mendell, c-Myc-regulated microRNAs modulate E2F1 expression, Nature 435 (2005) 839–843, https://doi.org/10.1038/nature03677.
[64] S. Li, Z. Liang, L. Xu, F. Zou, MicroRNA-21: a ubiquitously expressed pro-survival factor in cancer and other diseases, Mol. Cell. Biochem. 360 (2012) 147–158, https://doi.org/10.1007/s11010-011-1052-6.
[65] U. Kaukinen, S. Lyytikäinen, S. Mikkola, H. Lönnberg, The reactivity of phosphodiester bonds within linear single-stranded oligoribonucleotides is strongly dependent on the base sequence, Nucleic Acids Res. 30 (2002) 468–474, https://doi.org/10.1093/nar/30.2.468.
[66] U. Kaukinen, T. Venäläinen, H. Lönnberg, M. Peräkylä, The base sequence dependent flexibility of linear single-stranded oligoribonucleotides correlates with the reactivity of the phosphodiester bond, Org. Biomol. Chem. 1 (2003) 2439–2447, https://doi.org/10.1039/B302751A.
[67] U. Kaukinen, H. Lönnberg, M. Peräkylä, Stabilisation of the transition state of phosphodiester bond cleavage within linear single-stranded oligoribonucleotides, Org. Biomol. Chem. 2 (2004) 66–73, https://doi.org/10.1039/B309828A.
[68] R. Owczarzy, B.G. Moreira, Y. You, M.A. Behlke, J.A. Walder, Predicting stability of DNA duplexes in solutions containing magnesium and monovalent cations, Biochemistry 47 (2008) 5336–5353, https://doi.org/10.1021/bi702363u.
[69] C. Ragan, M. Zuker, M.A. Ragan, Quantitative prediction of miRNA-mRNA interaction based on equilibrium concentrations, PLoS Comput. Biol. 7 (2011) e1001090, https://doi.org/10.1371/journal.pcbi.1001090.
[70] J.-P. Shaw, K. Kent, J. Bird, J. Fishback, B. Froehler, Modified deoxyoligonucleotides stable to exonuclease degradation in serum, Nucleic Acids Res. 19 (1991) 747–750, https://doi.org/10.1093/nar/19.4.747.
[71] K.A. Lennox, M.A. Behlke, A direct comparison of anti-microRNA oligonucleotide potency, Pharm. Res. (N. Y.) 27 (2010) 1788–1799, https://doi.org/10.1007/s11095-010-0156-0.
[72] L.-H. Jiang, M.-H. Ge, X.-X. Hou, J. Cao, S.-S. Hu, X.-X. Lu, J. Han, Y.-C. Wu, X. Liu, X. Zhu, L.-L. Hong, P. Li, Z.-Q. Ling, miR-21 regulates tumor progression through the miR-21-PDCD4-Stat3 pathway in human salivary adenoid cystic carcinoma, Lab. Invest. 95 (2015) 1398–1408, https://doi.org/10.1038/labinvest.2015.105.
[73] X. Zhao, Y. Xu, X. Sun, Y. Ma, Y. Zhang, Y. Wang, H. Guan, Z. Jia, Y. Li, Y. Wang, miR-17-5p promotes proliferation and epithelial-mesenchymal transition in human osteosarcoma cells by targeting SRC kinase signaling inhibitor 1, J. Cell. Biochem. 120 (2019) 5495–5504, https://doi.org/10.1002/jcb.27832.
[74] D. Bautista-Sánchez, C. Arriaga-Canon, A. Pedroza-Torres, I.A. De La Rosa-Velázquez, R. González-Barrios, L. Contreras-Espinosa, R. Montiel-Manríquez, C. Castro-Hernández, V. Fragoso-Ontiveros, R.M. Álvarez-Gómez, L.A. Herrera, The promising role of miR-21 as a cancer biomarker and its importance in RNA-based therapeutics, Mol. Ther. Nucleic Acids 20 (2020) 409–420, https://doi.org/10.1016/j.omtn.2020.03.003.
[75] X. Bai, S. Hua, J. Zhang, S. Xu, The MicroRNA family both in normal development and in different diseases: the miR-17-92 cluster, BioMed Res. Int. 2019 (2019) 1–11, https://doi.org/10.1155/2019/9450240.
[76] Y. Zhu, J. Gu, Y. Li, C. Peng, M. Shi, X. Wang, G. Wei, O. Ge, D. Wang, B. Zhang, J. Wu, Y. Zhong, B. Shen, H. Chen, MiR-17-5p enhances pancreatic cancer proliferation by altering cell cycle profiles via disruption of RBL2/E2F4-repressing complexes, Cancer Lett. 412 (2018) 59–68, https://doi.org/10.1016/j.canlet.2017.09.044.
[77] V. Radulovic, T. Heider, S. Richter, S. Moertl, M.J. Atkinson, N. Anastasov, Differential response of normal and transformed mammary epithelial cells to combined treatment of anti-miR-21 and radiation, Int. J. Radiat. Biol. 93 (2017) 361–372, https://doi.org/10.1080/09553002.2016.1266057.
[78] D. Bose, S. Nahar, M.K. Rai, A. Ray, K. Chakraborty, S. Maiti, Selective inhibition of miR-21 by phage display screened peptide, Nucleic Acids Res. 43 (2015) 4342–4352, https://doi.org/10.1093/nar/gkv185.
[79] M. Hashemi, M.S.A. Mirdamadi, Y. Talebi, N. Khaniabad, G. Banaei, P. Daneii, S. Gholami, A. Ghorbani, A. Tavakolpournegari, Z.M. Farsani, A. Zarrabi, N. Nabavi, M.A. Zandieh, M. Rashidi, A. Taheriazam, M. Entezari, H. Khan, Pre-clinical and clinical importance of miR-21 in human cancers: tumorigenesis, therapy response, delivery approaches and targeting agents, Pharmacol. Res. 187 (2023) 106568, https://doi.org/10.1016/j.phrs.2022.106568.
[80] J. Sheu-Gruttadauria, P. Pawlica, S.M. Klum, S. Wang, T.A. Yario, N.T. Schirle Oakdale, J.A. Steitz, I.J. MacRae, Structural basis for target-directed MicroRNA degradation, Mol. Cell. 75 (2019) 1243–1255.e7, https://doi.org/10.1016/j.molcel.2019.06.019.
[81] I. Simeone, C. Rubolino, T.M.R. Noviello, D. Farinello, L. Cerulo, M.J. Marzi, F. Nicassio, Prediction and pan-cancer analysis of mammalian transcripts involved in target directed miRNA degradation, Nucleic Acids Res. 50 (2022) 2019–2035, https://doi.org/10.1093/nar/gkac057.
[82] D. Andreatta, S. Sen, J.L. Pérez Lustres, S.A. Kovalenko, N.P. Ernsting, C.J. Murphy, R.S. Coleman, M.A. Berg, Ultrafast dynamics in DNA: "fraying" at the end of the helix, J. Am. Chem. Soc. 128 (2006) 6885–6892, https://doi.org/10.1021/ja0582105.
[83] B. Schwanhäusser, D. Busse, N. Li, G. Dittmar, J. Schuchhardt, J. Wolf, W. Chen, M. Selbach, Global quantification of mammalian gene expression control, Nature 473 (2011) 337–342, https://doi.org/10.1038/nature10098.
[84] T.W. Turowski, D. Tollervey, Cotranscriptional events in eukaryotic ribosome synthesis, Wiley Interdiscip. Rev. RNA 6 (2015) 129–139, https://doi.org/10.1002/wrna.1263.
[85] C. Wang, T. Li, F. Yan, W. Cai, J. Zheng, X. Jiang, J. Sun, Effect of simvastatin and microRNA-21 inhibitor on metastasis and progression of human salivary adenoid cystic carcinoma, Biomed. Pharmacother. 105 (2018) 1054–1061, https://doi.org/10.1016/j.biopha.2018.05.157.
[86] B. Zhou, D. Wang, G. Sun, F. Mei, Y. Cui, H. Xu, Effect of miR-21 on apoptosis in lung cancer cell through inhibiting the PI3K/akt/NF-κB signaling pathway in vitro and in vivo, Cell. Physiol. Biochem. 46 (2018) 999–1008, https://doi.org/10.1159/000488831.
[87] Y.R. Wu, H.J. Qi, D.F. Deng, Y.Y. Luo, S.L. Yang, MicroRNA-21 promotes cell proliferation, migration, and resistance to apoptosis through PTEN/PI3K/AKT signaling pathway in esophageal cancer, Tumor Biol. 37 (2016) 12061–12070, https://doi.org/10.1007/s13277-016-5074-2.
[88] S.H. Javanmard, G. Vaseghi, A. Ghasemi, L. Rafiee, G.A. Ferns, H.N. Esfahani, R. Nedaeinia, Therapeutic inhibition of microRNA-21 (miR-21) using locked-nucleic acid (LNA)-anti-miR and its effects on the biological behaviors of melanoma cancer cells in preclinical studies, Cancer Cell Int. 20 (2020) 384, https://doi.org/10.1186/s12935-020-01394-6.